Final Draft
of the original manuscript:

Zhang, W.; Didenkulova , I.; Kurkina, O.; Cui, Y.; Haberkern, J.; Aepfler , R.; Santos , A.; Zhang, H.; Hanebuth, T.:
Internal solitary waves control offshore extension of mud depocenters on the NW Iberian shelf.
In: Marine Geology. Vol. 409 (2019) 15 - 30.
First published online by Elsevier: 27.12.2018

https://dx.doi.org/10.1016/j.margeo.2018.12.008

Internal solitary waves control offshore extension of mud depocenters on the NW Iberian shelf

Wenyan Zhang [a,*], Ira Didenkulova[b,c], Oxana Kurkina[b], Yongsheng Cui[d], Julia Haberkern[e], Rebecca Aepfler[e], Ana I. Santos[f], Han Zhang[g] and Till J.J. Hanebuth[h]

[a] *Institute of Coastal Research, Helmholtz-Zentrum Geesthacht, Max-Planck-Strasse 1, 21502 Geesthacht, Germany*
[b] *Nizhny Novgorod State Technical University n.a. R.E. Alekseev, Minina 24, Nizhny Novgorod 603950, Russia*
[c] *Department of Marine Systems, Tallinn University of Technology, Akadeemia tee 15A, Tallinn 12618, Estonia*
[d] *Center for Coastal Ocean Science and Technology, Sun Yat-sen University, 510275 Guangzhou, China*
[e] *MARUM – Center for Marine Environmental Sciences, University of Bremen, 28359 Bremen, Germany*
[f] *Marinha – Instituto Hidrografico, Lisbon, Portugal*
[g] *State Key Laboratory of Satellite Ocean Environment Dynamics, Second Institute of Oceanography, Hangzhou, China*
[h] *Department of Coastal and Marine Systems Science, Coastal Carolina University, Conway, SC 29528, U.S.A.*

[*] Corresponding author: wenyan.zhang@hzg.de, Tel: +49 (0)4152 87 1568

Abstract

Hydrodynamic conditions and near-bottom sediment transport on the NW Iberian shelf associated with a 5-day storm in September 2014 were monitored. During the post-storm relaxation period, active bottom sediment transport by internal solitary waves (ISWs) on a mid-shelf mud depocenter, located in between 110 and 130 m water depth (WD), was observed. To explore the potential of internal waves in sediment transport and its link to development of mid-shelf mud depocenters, we apply a weakly nonlinear model based on the variable-coefficient Gardner equation to estimate the flow fields and bottom shear stress induced by shoaling of mode-1 long internal solitary waves. Shoreward propagation of the ISWs in three representative periods (pre-, intra- and post-storm) is simulated, respectively. Transformation of the internal wave, from a single sech^2 shape characterized by negative polarity and small amplitude to a dispersive trailing wave packet with varying amplitude and inverse polarity, are satisfactorily reproduced. Model results indicate enhancement of the maximum orbital velocity of the ISWs during and after the storm on the outer shelf (130-220 m WD) including the seaward margin of the mud

depocenter. Bottom shear stress consequently becomes strong enough (>=0.1 Pa) to winnow unconsolidated sediment and constrains the offshore extension of the depocenter. The enhanced bottom orbital velocity and the asymmetry in the excursion direction of mode-1 long ISWs in the post-storm period prove to be efficient in transporting fine-grained sediment across shelf. Our results suggest that mid-shelf mud depocenters are not necessarily areas under permanently calm conditions where fine-grained sediment can settle straightforwardly. They could also result from convergent sediment transport from both onshore and offshore directions, and sediment may go through numerous cycles of resuspension-transport-deposition before its ultimate lasting burial.

Keywords: Shelf processes; numerical modeling; field instrumentation; North Atlantic; sediment transport

1. Introduction

Coastal and continental shelf mud depocenters (MDCs hereafter) are an important sink for continent-derived material during modern sea level highstand conditions. They serve as habitat for benthic life and store large quantities of organic carbon, nutrients, and contaminants (e.g. Hedges and Keil, 1995; Blair and Aller, 2012; Mahiques et al., 2016). Despite of their important role in the global source-to-sink connection and ecosystem functioning, their formation dynamics as well as the particular natural and anthropogenic drivers that shape their morphology remain poorly understood (e.g. Walsh and Nittrouer, 2009; Hanebuth et al., 2015a; Zhang et al., 2016). Three processes, namely 1) surface buoyancy plume related to river discharge, 2) dilute suspension dispersal in the bottom-boundary layer, and 3) gravity-driven turbidity flows have been identified as being responsible for the transport of fine-grained sediment across continental shelves (e.g. Cacchione et al., 1987; Bursik, 1995; Syvitski and Morehead, 1999; Ogston et al., 2000; Traykovski et al., 2000, 2007; Hill and McCave, 2001; Geyer et al., 2004; McKee et al., 2004; Walsh and Nittrouer, 2009; Hale and Ogston, 2015; Zhang et al., 2016). The latter two processes are particularly critical for the formation of MDCs (e.g. McCave, 1973; Ogston et al., 2000; Wright and Friedrichs, 2006; Wu et al., 2016).

Until recently, internal waves were suggested to be another important process for resuspension and transport of fine-grained sediment across continental shelves (e.g. Johnson et al., 2001; Quaresma et al., 2007; Bourgault et al., 2014; Cheriton et al., 2014). Formation of certain sediment wave fields such as those on the shelf of NW Mediterranean was hypothesized to result from shoaling of internal waves (van Haren and Puig, 2017). Deep

penetration of internal solitary waves (ISWs) was promoted by seasonal deepening of stratification, allowing the ISWs to rework mid-shelf sediments and possibly form sediment waves that are characterized by similar wavelengths to the ISWs. Some geological studies in addition suggest that certain stratigraphic structures found in sedimentary rocks, such as hummocky-cross stratification layers, may result from the impact of internal waves (e.g. Morsilli, M., and Pomar, 2012; Pomar et al., 2012).

The mechanism, which acts when internal waves cause sediment resuspension, is related to wave deformation during shoaling, as demonstrated in both laboratory and numerical experiments (e.g. Hosegood et al., 2004; Boegman and Ivey, 2009; Bourgault et al., 2014; Lamb, 2014). Bottom shear stress is enhanced by interaction between internal waves and seafloor during shoaling and can become strong enough to trigger the movement of unconsolidated fine-grained sediment particles by means of rolling, saltation, and suspension. Particles are further lifted up by vertical movements associated with turbulent vortices generated during the wave deformation. While larger particles re-deposit rapidly as a result of decay of the turbulent boluses, fine-grained sediment entrained in the mixed fluid around the pycnocline may be advected further offshore (Richards et al., 2013; Bourgault et al., 2014). This process leads to the formation of intermediate nepheloid layers that are frequently observed at continental margins worldwide (e.g. Cacchione and Drake, 1986; McCave et al., 2001; Oliveira et al., 2002; McPhee-Shaw et al., 2004).

The relationship between intermediate nepheloid layers and MDCs is complex, because their formation might be decoupled from each other (Palanques and Biscaye, 1992). Recent observations indicate that resuspension and subsequent along-isopycnal dispersal of mud by internal waves at the outer shelf, especially by long waves such as internal tides, can be important in defining the location of MDCs, and might even feed their growth by shoreward material transport toward the middle and shallow section of the mud deposits (e.g. Inthorn et al., 2006; Cheriton et al., 2014). While the impact of internal waves on dispersal and sedimentation of mud have been supported by numerical and lab experiments, considerable gaps in our understanding of the natural system still exist, especially in the quantification of sediment fluxes (Bourgault et al., 2014). Under which circumstances internal waves are able to produce indicative textural sedimentation patterns that may be preserved in sedimentary rocks and soft sediment cores remains unclear as well, given the fact that formation of such sediment structures requires either persistent forcing over a long period or the preservation of a major storm event horizon, while

internal waves are highly variable on both temporal and spatial scales (Shanmugam, 2013).

The purpose of our study is to derive further insights into the impact of mode-1 (i.e. two-layer structured) long ISWs on MDCs. Our study area is the northwest Iberian continental shelf which hosts a series of MDCs (Fig. 1). Hydrodynamic conditions and near-bottom sediment transport associated with a 5-day storm in September 2014 were monitored by a research cruise. The monitoring covered the entire phase of a downwelling-inducing storm passing through the study area, i.e., from pre-storm to post-storm period. An earlier study by the authors focusing on the pre- and intra-storm periods found that strengthened oceanic density front by storm-induced downwelling and the associated jet flow along the coastline imposed a primary control on transport and deposition of fine grained sediment on the inner shelf (20-110 m WD) of the study area and confined the shoreward boundary of shelf MDCs (Zhang et al., 2016). Enhanced current-wave interaction during the storm was able to produce gravity-driven turbidity flows in various muddy areas of the shelf, and contributed to deposition on the MDCs. The field data derived from the second cruise phase, i.e., the post-storm period, indicate an active role of long ISWs in sediment transport across the seaward boundary of MDCs, and therefore are in the focus of the present study.

2. Regional setting

Our study area is located off the northwest Iberian Peninsula in northeast Atlantic. It is characterized by a relatively narrow shelf (width within 40 km) and a steep (> 20°) continental slope (Fig. 1). The physical oceanographic conditions in this region are mainly controlled by the Eastern Boundary Currents along the shelf edge and local wind-driven currents on the shelf (Relvas et al., 2007). The shelf edge current system is characterized by a slow, broad equatorward circulation at the sea surface (within ~100-150 m WD) and poleward compensating flows below (~100-600 m WD). The shelf dynamics are mainly controlled by a seasonal variation of two major atmospheric systems: the Azores High and the Iceland Low (Wooster et al., 1976). As a result two mean circulation patterns, with summer upwelling from April to September and winter downwelling from October to March, develop with inter-annual variability in the intensity and timing. In contrast to a relatively calm hydrodynamic condition characterized by a mild equatorward current and low-energy waves with height typically below 3 m, the hydrodynamic regime on the shelf in winter becomes energetic, characterized by episodically strong poleward wind-driven currents and increasing wave heights (PO-WAVES Group, 1994). Significant wave heights often exceed 5 m during winter storms. Interaction between swells and storm-generated local waves can produce maximum wave

heights over 10 m on the mid-shelf (Vitorino et al., 2002). Heavy precipitation often accompanies winter storms and results in extreme river runoff values (Otero et al., 2010).

Monitoring data of a storm which hit the NW Iberian shelf from 15 September to 20 September 2014 clearly demonstrate a dominant control on sediment transport and redistribution across the entire shelf by energetic events (Zhang et al., 2016). Strong southerly winds (up to 25 m/s) accompanying the storm front effectively drove the surface water towards the coast and resulted in a prominent downwelling on the inner and mid-shelf. The mid-shelf thermocline, originally located between 20 and 35 m WD, was depressed down to 50-60 m depth during the storm. Due to a large density difference between the surface and bottom waters, a strong positive buoyancy was generated at the interface between the downwelling and bottom water, producing a vertical density front characterized by a large across-shelf density gradient. The oceanic density front was located in about 80 m depth in the south (off the Douro river mouth) and gradually deepening to 120 m in the north of the study area (off the Ría de Vigo). A jet-like coastal current developed at the shoreward side of the front with current velocities higher than 0.25 m/s near the seafloor, while the seaward side of the front was relatively calm with near-bottom (calculated at 0.005 *D* above seafloor, where *D* is local water depth) current velocity less than 0.1 m/s. Active bottom sediment resuspension (concentration higher than 0.4 kg/m^3 at 150 cm above seafloor) was observed on the inner shelf (73 m WD) at the edge of a mud depocenter off the Douro river mouth and transported toward the depocenter. It was found that storm-generated downwelling front and associated coastal jet impose a primary control on transport and deposition of fine-grained sediment on the shelf. Intra-storm transport and post-storm deposition of highly-concentrated near-bottom sediment suspensions (>10 kg/m^3) generated by wave-current interaction and flow convergence in local muddy sites are suggested to contribute to deposition on MDCs of the study area. In additional to the hydrographic control on sediment transport and deposition by storms, topographic relief associated with the rocky outcrops on the outer shelf in the southern part of the study area (Fig. 1) is suggested to play an important role in constraining a seaward expansion of several MDCs in the region (Dias et al., 2002). These rocky bedrocks are several meters high and act as a barrier widely hindering offshore sediment dispersal. As a result, the MDCs in the southern part of the study area is restricted to the zone between the front and the rocky outcrops (Zhang et al., 2016). The driving mechanism for a well-defined seaward boundary of

MDCs in the northern part of the study area (off the Rias, Fig. 1), where topographic influence by rocky outcrops is absent, is yet unclear.

Besides energetic surface gravity waves produced by winter storms, ISWs are frequently observed in the Iberian shelf waters by both satellite images and hydrographic moorings (e.g. da Silva et al., 1998; Quaresma et al., 2007; Magalhaes and da Silva, 2012). ISWs have been found to significantly enhance dissipation rates of turbulent kinetic energy and vertical diffusivity on the shelf edge of NW Iberia (Barton et al., 2001). Although strengthened stratification in summer promotes development of ISWs along the thermocline, active ISWs in winter months in the study area have also been reported (Varela et al., 2005). Observations indicate that episodically enhanced ISWs have the power to remobilize mid-shelf bottom sediments (Quaresma et al., 2007). Despite evidence of capability of ISWs in matter transport in this region, their action and role in development of MDCs remain unexplored.

3. Materials and methods

3.1. Field measurements

Field data in the study area are mainly derived from the research cruise M110 GALIMOS (Monitoring the interaction between Oceanographic elements and Sedimentary seabed structures at the GALIcian margin; 14-30 September, 2014, with the German R/V METEOR). Work report of the cruise is provided by Hanebuth et al. (2015b), with its first scientific results reported by Zhang et al. (2016). The cruise was performed in two phases, with the first in Portuguese waters (south of 42°N) from 16 September (before arrival of the storm front) to 20 September (right after the passing through of the storm) to monitor the storm impact on the MDCs, and the following in Spanish waters (north of 42°N) from 21 to 26 September to monitor the sediment dispersal and deposition on the MDCs in the post-storm relaxation period. Besides 58 vertical CTD (Conductivity, Temperature, Depth) profiles at 42 stations along nine cross-shelf tracks (denoted as P0-P6 in Portuguese water and S1-S2 in Spanish water, see Fig. 1b), 78 water samples were collected shipboard. Furthermore, a seafloor lander equipped with various sensors including Electromagnetic Current Meters (ECM), CTD, Optical Backscatter Sensors, two Acoustic Doppler Current Profilers (300 and 1200 kHz, respectively) and a Laser In-Situ Scattering and Transmissiometry (LISST) was deployed at a muddy sand site (73 m WD, ~30% mud) off the

Douro river mouth (Figure 1b) in the first cruise phase (16-20 September) and at the Galician mud depocenter (127 m WD, ~85% mud) off the Ría de Vigo (Fig. 1b) in the following cruise phase (21-26 September). The upward-looking 300 kHz ADCP operated continuously and provided average data for every 600 s. Its bin size was set to 2 m and covered a vertical range of ~97 m above the lander at the Galician mud depocenter. The downward-looking 1200 kHz ADCP unfortunately malfunctioned and failed to record any data during the cruise. The ECMs operated continuously and provided data at a frequency of 4 Hz. A nearly continuous record of acoustic backscatter data from the water column was collected using the 18 kHz primary high frequency from the hull-mounted Parasound P70 (Atlas Hydrographic) Echo sounder. During the acquisition of dedicated hydroacoustic profiles (see Figure 1b) a constant route speed of 3.34 m/s (i.e. 6.5 kn) was maintained.

3.2. Numerical modeling of internal solitary waves

A weakly nonlinear model based on the variable-coefficient Gardner equation (Holloway et al., 1999; Grimshaw et al., 2010; Talipova et al., 2014) is applied in this study to simulate the shoreward propagation of internal waves in a two-dimensional vertical plane (2DV). The variable-coefficient Gardner equation is an extended Korteweg-de Vries (eKdV) equation (Korteweg and de Vries, 1895) including cubic nonlinearity to take into account internal waves of large amplitude (Grimshaw et al., 2004). An advantage of the model is that it allows very high resolution calculations with small computational expense and in the meanwhile is able to provide results similar to sophisticated nonhydrostatic models (O'Driscoll and Levine, 2017; Yuan et al., 2018). Another advantage of this model is that it is able to capture the dynamics of long internal waves during their shoaling in coastal and shelf waters with inhomogeneous stratification along both the horizontal and vertical axis (e.g. Grimshaw et al., 2004, 2010; Talipova et al., 2014). Major equations of the model are described below. For further mathematical details the reader is referred to Holloway et al. (1999), Grimshaw et al. (2004) and Talipova et al. (2014).

The variable-coefficient Gardner equation with inclusion of bottom friction and Earth's rotation effect is described by

$$\frac{\partial \eta}{\partial t} + (c + \alpha\eta + \alpha_1\eta^2)\frac{\partial \eta}{\partial x} + \beta\frac{\partial^3 \eta}{\partial x^3} = \frac{f^2}{2c}\int \eta dx - (\nu|\eta| + \frac{c}{2Q}\frac{dQ}{dx})\eta\,, \qquad (1)$$

where η is the maximum vertical displacement of the pycnocline that varies with time (t) and distance (x) from the initial position (x = 0), c is the wave phase speed, α and α_1 are quadratic and cubic nonlinear coefficients, respectively, β is a dispersion parameter, f is the Coriolis frequency, ν is a bottom friction coefficient and Q is an amplification factor in the linear long-wave theory due to changes in the water depth and stratification. The three terms on the right hand side of the equation stand for the impact of Earth's rotation, bottom friction and changes of water depth and stratification during shoaling, respectively.

The wave speed c is determined from the eigenvalue problem for the modal structure function $\phi(z)$ of the vertical displacement in the linear long-wave limit adopting the Boussinesq approximation and the rigid-lid boundary condition (i.e. $\phi(0) = \phi(-H) = 0$, where -H is the seafloor depth):

$$\frac{d}{dz}\left\{[c - U(z)]^2 \frac{d\phi}{dz}\right\} + N^2(z)\phi = 0, \tag{2}$$

where $U(z)$ is the background horizontal current velocity, and $N(z)$ is the undisturbed background buoyancy frequency (provided by the 3D coastal ocean model in this study). Note that Eq. (2) defines an infinite sequence of regular modes with corresponding speeds. We only focus on the mode 1 function, that is, $\phi(z)$ has its maximum at $z_{\max}$ in the interior of the water. $\phi(z)$ is then normalized by $\phi(z) = \phi(z)/\phi(z_{\max})$.

Once $\phi(z)$ and c are known, other parameters in Eq. (1) that depend on them, such as the nonlinear coefficients α and α_1, the dispersion parameter β, the bottom friction coefficient ν and the amplification factor Q can be derived. Numerical details are provided in Grimshaw et al. (2004, 2010).

The density $\rho(x,z)$ and current velocity fields ($u(x,z), w(x,z)$) associated with the motion of the internal waves are then given by

$$\rho(x,z) = \rho(x, z - \eta(x)\phi(z)), \tag{3a}$$

$$u(x,z) = c\eta(x)\frac{\partial\phi(z)}{\partial z}, \tag{3b}$$

$$w(x,z) = -c\phi(z)\frac{\partial\eta(x)}{\partial x}. \tag{3c}$$

It is worth to note that bottom friction may significantly influence the near-bottom velocity field of internal solitary waves (e.g. Kurkina et al., 2016). It has been found that a reverse horizontal flow forms directly behind the main flow generated by a solitary wave. This reverse flow is confined near the bottom and is hypothesized to be generated by a balance between bottom friction and pressure (Kurkina et al., 2016). Although being much weaker than the main horizontal flow associated with a solitary wave (described by Eq. 3b), the reverse flow may play an important role in transporting sediment that is resuspended by a preceding strong main flow. The near-bottom flow reversal is not resolved in the model due to the simplification in the equation which does not take into account the balance between pressure and bottom friction. However, we attempt to discern such reverse flow in our monitoring data and discuss its potential impact on sediment transport. Within the main flow field associated with a solitary wave, the bottom shear stress $\tau(x)$ is estimated from a combined effect of the internal wave motion and the background flow using the law of the wall:

$$\tau = \rho\{\kappa[u(z_r)+U(z_r)]/[\ln(z_r+H)-\ln z_0]\}^2, \quad (4)$$

where κ (=0.4) is the von Karman constant, $z_r = 10 - H$ refers to 10 m above the seafloor and z_0 is a reference height above the seafloor where current velocity is assumed to be zero. z_0 is also called bottom roughness length and its value for the mud deposits with a relatively flat surface is given by $z_0 = 2.5d_{50}/30$, where d_{50} is the median grain size of the seafloor sediment (Zhang et al., 2016).

3.3. Model setup for the study area

In order to figure out the temporal and spatial variability of the internal waves and their potential in remobilizing seafloor sediment, we set up a 2DV model domain for the cross-shelf profile S1 with horizontal and vertical spatial resolution of 100 and 0.05 m, respectively. The computational time step is 5.5 s. The profile extends from the continental slope at 1000 m WD to the inner shelf at 50 m WD, with a horizontal length of 62 km. A sech^2 shape internal wave with negative polarity (because both the quadratic and cubic nonlinear coefficients have negative values here) is introduced at the open ocean boundary as an initial disturbance of the density field. The maximum vertical displacement of the pycnocline (η) by the wave at the seaward boundary is set to 15 m and its initial period to 6000 s according to measurements at a stationary station located on the

continental slope (station 32 in Fig.1). This open boundary condition is imposed periodically in a M_2 tidal cycle (12.42 hrs) to be consistent with the field observation. Shoreward propagation and transformation of this wave in three representative periods (pre-, intra- and post-storm) is simulated, respectively.

The background density fields for the internal wave model are derived from simulation results by a validated 3D coastal ocean model (Zhang et al., 2016). A comparison between the simulation results and observed data (vertical CTD profiles) suggests an overall satisfactory model performance. Despite of a reduction of the density gradient across the pycnocline by ~15%, the temporal and spatial variation of both water layers (separated by the pycnocline) are well reproduced by the 3D model. The deviation of the density gradient across the pycnocline is mainly related to an overestimation of the temperature beneath the pycnocline in the model, which is about 2 °C higher than the observed data (Zhang et al., 2016). The effect of the reduced density gradient across the pycnocline on the 2DV internal model results has been tested by sensitivity runs which indicate only a minor effect (within 11% deviation) on the amplitude of ISWs and thus does not affect interpretation of the results.

4. Results and analysis

4.1. Field observation

4.1.1. Post-storm conditions – currents

In the afternoon of 20 September the wind weakened rapidly, combined with decreasing seas and shower activity. The following six days (21–26 September) was relaxation period characterized by a weak wind strength between 2 to 6 m/s and reversal in the wind direction from southerly to northerly. The surface wind wave height was mostly below 1.5 m and dominated by swells with a period of about 8 s. The rapid decrease of wind velocity in the first 30 hours (till the end of 21 September) resulted in a rebound of the bottom cold water toward the inner shelf. This is evidenced by a comparison of vertical density profiles at CTD stations between two neighbouring cross-shelf track lines measured in intra- and post-storm periods, respectively (Fig. 2, with location of the track lines in Fig. 1). Lander observation located off the Ría de Vigo, which shows a drop of temperature by 0.15 °C from 12:00 UTC 21 September to 00:00 UTC 22 September and an increase of water density by about 0.3 kg/m^3, further confirms the shoreward migration of denser bottom water (Fig. 3a). After the initial change the bottom

water temperature and salinity remained stable at the monitoring site. Recorded 600 s average current time series by the upward-looking ADCP indicate a complicated hydrodynamic regime on the mid-shelf (Fig. 3). In most of the monitoring period (in total 79.5 hrs from 21 to 24 September) the vertical current above the Galician mud depocenter exhibited a two-layer structure, with stronger current intensity in the surface layer. Besides high-frequency oscillations, a semidiurnal (M_2) tidal undulation is clearly seen in the signal (Fig. 3). The M_2 tidal ellipse at this site is relatively narrow and aligned mainly along the NNE (15°) – SSW (195°) axis. Butterworth band-pass filtered data indicate that the tidal current velocity oscillates between $\pm$ 0.06 m/s. The enhanced current intensity resulted from a combined effect of tides and high-frequency oscillations characterized by periods between 15-30 min and a two-layer (i.e. with opposite current directions) vertical structure (Fig. 3e). It is particularly worth to note that the high-frequency oscillations were aligned mainly along the west-east axis (Fig. 4a) and characterized by a stronger and longer-lasting offshore directed component (i.e. negative *u*) (Fig. 3e). They altered both current strength and direction along the west-east axis (Fig. 3e), while their effect along the south-north axis was relatively small (within $\pm$ 2 cm/s according to high-pass Butterworth filtering of the 600 s average data) and did not reverse the current direction (Fig.3d). Although the high-frequency oscillations consistently appeared in the entire monitoring period, only in certain circumstances their strength was enhanced (> 5 cm/s in the 600 s average data) (Fig. 3e). Another phenomenon worth to note is that the mean current (600 s average) within a few (7-9) meters above the seafloor behaved differently than that in the upper water column. This behavior is not only due to a bottom Ekman spiral effect (Zhang et al., 2016) but also associated with the high-frequency oscillations. Reverse and relatively weak currents (< 2 cm/s) appeared within a few meters above the seafloor after strong offshore-directed high-frequency currents and lasted considerably long (Fig. 3e).

Information from the near-bottom (20 and 150 cm above seafloor, respectively) ECM data (4 Hz) indicates that the strong high-frequency oscillations (> 0.2 m/s) occurred mainly at low tide (Fig. 4). These oscillations proceeded mainly along the west-east axis (Fig. 4a and 4b). Calculation of current energy spectra in three selected time slices at low tide identifies two dominant wave groups, one centering at about 100 s and the other between 1000 and 1400 s in period (Fig. 5). However, in contrast to the 100 s group which shows a high peak in the power spectral density of pressure, the long wave group exhibits a much weaker peak in the pressure signal (Fig. 5d).

Because the frequency of internal waves is limited by the buoyancy frequency N, which was observed above the outer and inner margins of the MDC during the post-storm period to range between 2×10^{-3} s^{-1} (= 500 s in period) and 7×10^{-3} s^{-1} (=143 s in period), respectively, the possibility of the 100 s group being internal waves can be discarded. These results suggest that the 100 s wave group comprises surface gravity waves (i.e. infragravity waves) while the long wave group refers to internal waves that were observed as high-frequency (period between 15-30 min) oscillations (e.g. Moum and Smyth, 2006). The infragravity waves are consistently seen in the time series and induced a flow oscillation within ± 0.03 m/s at the lander, while the internal waves were enhanced at low tide and caused change of the near-bottom current velocity by max. 0.3 m/s. The duration of each strong internal wave pulse lasted for about 6 hrs at the lander site. A combination of the ADCP and ECM datasets indicates the presence of cyclically enhanced mode-1 long internal waves above the Galician MDC in the post-storm period.

4.1.2. Post-storm conditions – near-bottom SPM transport

Vertical profiles of SPM concentration at the CTD stations indicate that turbidity was very low in the upper water column and SPM became increasingly abundant toward the seafloor (Fig. 2). A pronounced enhancement of the near-bottom (within 10 m above seafloor) SPM concentration was monitored above the seaward margin of the MDC in intra- and post-storm periods (at Station 13 and 37, see Fig. 2), further proving a persistent active sediment transport across the MDC. It is worth mentioning that the SPM concentration above the seaward margin of the MDC was higher in the post-storm period compared to that during the storm, and also higher than the observed value above the shoreward margin of the MDC. Recorded time series of near-bottom (30 cm above seafloor) SPM on the Galician MDC indicate that SPM concentration started to rise at 00:00 UTC on 22 September (Fig. 4), right after the initial increase of bottom water density (Fig. 3a). Maxima of SPM concentration appeared in short-lasting pulses, which were similar to the appearance of enhanced internal waves (Fig. 4c). However, the changes of these two quantities were only weakly correlated (Pearson's r = 0.12), suggesting that a major portion of the SPM at the lander site was not produced by local resuspension. Furthermore, a forward shift of 8 hrs in the SPM data results in a high correlation coefficient (r = 0.89) with the bottom current velocity (Fig.4d). This indicates that the near-bottom SPM at the nucleus of the MDC, where the

lander is located, mainly originated from a remote source where strong internal waves occurred few hrs earlier (than at the lander site). The grain size composition (Fig. 4e) indicates that the SPM was mostly composed of coarse silts and fine sands (i.e. 50-200 μm) and exhibited a decreasing trend in grain size with time. This is significantly different from the grain size spectrum observed during the storm (off the Douro river mouth, location in Fig. 1) which shows a remarkable portion of flocs ("marine snow") characterized by grain size larger than 200 μm (Zhang et al., 2016). Analysis of seafloor surface sediment samples however, indicated a dominance of medium silts (6-20 μm) which made up more than 70% at this site. The mismatch in grain size between the SPM and the seafloor sediment *in situ* further indicates that the SPM has an origin from the margin of the MDC where sediment is coarser.

It is worth to note that the power spectral density of turbidity recorded by the ECM shows a clear signal at the frequency of the internal waves during low tide (Fig. 5e and 5f). Calculation of the near-bottom (30 cm above seafloor) sediment transport flux ($=uC$, where C is SPM concentration) induced by internal waves is derived through a band-pass filtering (cut-off frequencies are 2.5×10^{-3} and 2.5×10^{-4} Hz, respectively) of the original times series from the ECM. Results from three selected time slices at low tide (Fig. 6) indicate a net onshore transport by enhanced internal waves. The residual transport fluxes in time slice 1 (5-9 h), 2 (27-31 h) and 3 (66-70 h) are 126, 520 and 267 g s^{-1} m^{-2}, respectively. A combination of information above leads to the conclusion that a lasting sediment resuspension from the outer shelf and subsequent transport toward the nucleus of the MDC was initiated by enhanced internal waves in the post-storm period..

4.1.3. Cross-shelf acoustic backscatter profiles

The echograms (18k Hz) along different cross-shelf track lines reveal that plenty of internal wave-like reflectors were present during the entire cruise (Fig. 7). Three major types of reflectors, which reoccurred at specific water depths throughout the cruise, are identifiable (Fig. 7a). Type 1 and 2 appeared in shallower water between 20 and 150 m WD, while type 3 was located in deeper water (200-300 m WD) and most prominent at the shelf edge. Type 1 reflectors overlapped with the thermocline. They exhibited a relatively symmetric shape with wave length between a few hundred and a few thousand meters and period between a few minutes and a few hours on the continental rise before approaching the slope, and became progressively asymmetric with both

decreasing wave lengths and periods when propagating toward the inner shelf. Compared to type 1 reflectors that are restricted to the upper water column, type 2 reflectors are in close contact with the seafloor and are connected to type 1, as seen from the echograms (e.g. P5 and P1 in Fig. 7). Type 2 reflectors existed only on inner and mid-shelf. They exhibited large amplitudes (30-80 m), short wave lengths (200-1000 m) and an asymmetric shape with a pronounced positive polarity. Note that the wave lengths of these reflectors are underestimated in the echograms due to the Doppler effect created by the ship movement toward the shelf edge.

It is worth to mention that an acoustic profile illustrating a plume of high backscatter intensity confined to a certain water depth range (120-180 m) on the mid- and outer shelf was detected in the post-storm period (21 September) along track line S2 (Fig. 7d). This plume probably consisted of resuspended SPM originated from actions of internal waves on the outer and mid-shelf seafloor. The vertically confined thickness of the plume indicates a stable along-isopycnal dispersal with limited vertical mixing.

4.2. Simulation results

4.2.1. Model validation

Generally, the modeled vertical displacement of the pycnocline (η) along Profile S1 is in good agreement with the amplitude of internal reflectors identified in the echogram (Fig. 8). The modelled period of internal waves above the lander site varies between 1600 s for the leading waves and 750 s for the trailing waves, which is close to the field data (Fig. 8c). The modeled horizontal velocity induced by the internal waves without bottom friction effect is higher than the ADCP data at 100 m WD and the band-pass filtered ECM data at 1.5 m above the sea floor. This is not surprising because the ADCP data are 600 s averaged in which peaks are smoothed, while the ECM data are within the bottom boundary layer that is strongly affected by friction. The shoaling and transformation of the ISWs from an initial sech^2 shape characterized by negative polarity and small amplitude (η = 15 m) to a trailing wave packet with varying phase speed and amplitude, are satisfactorily reproduced. The trailing packet is led by a pulse of large amplitude and high frequency solitary waves with positive polarity (Figure 8 and 9). Model results also indicate significant differences in the transformation of the ISWs in three periods (pre-, intra- and post-storm, example given in Fig. 9). The most remarkable difference of ISWs in these three periods is the location of a critical point where the weak nonlinearity is destroyed and model simulation

terminates (Fig. 9). For a better comparison with the lander data, we focus on the simulation result for the post-storm period. A discussion of the differences in the three periods and their general implication is given in section 5.

4.2.2. Simulated internal waves in the post-storm period

The spatial variation of the coefficients in the 2DV model along S1 in the post-storm period is shown in Fig. 10. The model computation terminates at mid-shelf water (8.96°W in longitude), where the leading ISW becomes unstable and its weakly nonlinearity no longer holds due to a drastic increase of higher order nonlinear terms. The results show that the linear long wave speed c decreases from 1.2 m/s at the open boundary to 0.26 m/s at the mid-shelf (110 m WD). The coefficient of the cubic nonlinearity α_1 experiences several changes of its sign along the propagation of the ISWs, each resulting in a change in the amplitude of the ISW (Fig. 11). Because the cubic nonlinearity ($\alpha_1\eta^2$) is weak and α is relatively stable, the initial internal wave maintains a soliton-like shape before it approaches the shelf edge (Fig. 11). After crossing zero above the shelf edge α_1 remains negative until reaching another critical point at the mid-shelf (164 m WD, 9.1°W in longitude) where it crosses zero again. During this course the polarity of the ISWs is exclusively determined by the sign of α (Grimshaw et al., 2004), which changes from negative to positive. This indicates that the polarity of the ISWs changes correspondingly from negative to positive (Fig. 11). The Earth's rotation term is not shown in Fig. 10, but can be found from c and the Coriolis frequency f (=0.976 $\times 10^{-4}$ rad/s in our study area). It is easy to judge from Eq. (1) that this term has significant effect only on waves with period larger than the inertial ones ($2\pi / f$ = 17.88 hrs in our area), thus its effect on the ISWs is much smaller than other terms described earlier. According to model sensitivity study, the Earth's rotation decreases the amplitude of the leading wave by less than 10%, and slightly reduces the number of trailing waves in our study area. The bottom friction term is found to be of minor importance until where the amplitude of the leading ISW becomes considerably large (> 40 m).

The ISW remains in the soliton-like shape until reaching the shelf edge, and deformation starts afterwards (Fig. 11). A lengthening trailing tail develops behind the leading wave and a dispersive wave packet forms. Because part of the energy in the initial internal wave is lost to the trailing tail, the amplitude of the leading wave decreases from ~30 m to ~23 m in the first few km from the shelf edge towards the coast. The leading wave

391 propagates faster than the trailing waves which have the phase speed of c. At the critical point (~9.28°W) where
392 α changes its sign from negative to positive, the wave polarity starts deformation accordingly. The amplitude of
393 the leading wave increases after a change of its polarity, in the meanwhile the wave length becomes continuously
394 smaller due to a conservation of the wave energy. Behind the leading wave the isopycnal is elevated and steepens
395 due to an increased amplitude of the leading wave. This results in a disintegration of the trailing tail into a wave
396 train with an increasing number of waves. It should be noted that although the amplitude of the trailing waves is
397 independent from the initial solitary wave amplitude η_0, the wave number and formation rate of each trailing
398 wave do depend on η_0, because the wave momentum should be conserved (Grimshaw et al., 2004). The
399 amplitude of the leading wave reaches its maximum (~80 m) at 8.976°W, where the seafloor depth is 116 m. This
400 is a critical point where α_1 crosses zero and becomes positive afterwards. Here the quadratic nonlinear term ($\alpha\eta$
401) exceeds the linear long wave speed c and the weak nonlinearity is destroyed. Transformation of the leading
402 wave is dominated by higher order nonlinearity afterwards, which is not resolved by the 2DV model. Although
403 development of the exceptionally large amplitude of the leading wave is beyond the applicability of the weakly-
404 nonlinear assumption of the 2DV model, similar waves with smaller amplitude (~50 m) were indeed reflected in
405 the echograms (Figure 7a, 7c and 7e). This good agreement implicates that our model is capable of reproducing
406 the essential features of the field observations. Breaking and intense mixing should occur in the shoreward
407 direction of the large amplitude leading waves, according to the criterion that the local Ostrovsky number (
408 $O_s = 2\alpha^2\eta^2 c\beta^{-1} f^{-2}$, see Eq.(35) and (36) in Grimshaw et al. (2014)) exceeds 1. Furthermore, the maximum
409 horizontal orbital velocity $u(x,z)$ exceeds the wave phase speed c at this point (Fig. 11 and 12), also indicating
410 a potential breaking afterwards (Vlasenko and Hutter, 2002).

411 **4.2.3. Flow asymmetry and bottom shear stress**

412 Simulations indicate that the horizontal orbital velocity $u(x,10-H)$ of the ISWs at 10 m above seafloor
413 increases in an accelerated rate after passing through the critical point (α) at 9.21°W, where the seafloor depth is
414 180 m (Fig. 11 and 12). This is induced by a combined effect of increased amplitude (η) and vertical gradient of
415 the modal structure function $\phi(z)$, as implemented in Eq.(3b). An asymmetry in both the strength of

416 $u(x,10-H)$ and duration of the orbital excursion, with a more pronounced offshore directed component, is
417 clearly seen (Fig. 11 and 12). This is also consistent with the field measurement showing a dominant offshore
418 component above 10 m from the seafloor (Fig. 2e). It can be easily deduced from Eq.(3b) that the asymmetry in
419 the strength of $u(x,10-H)$ is related to the ratio of the depth where $\phi(z)$ reaches its maximum (z_{max}) to the
420 entire local water depth ($-H$). Accordingly, the offshore directed component becomes increasingly pronounced
421 when z_{max} is deepened. The asymmetry in the duration of the orbital excursion is attributed to deformation of the
422 ISWs during their shoaling, which results in a narrowing of the wave crest and broadening of the wave trough
423 (Fig. 11a). Assuming that the critical shear stress for resuspension of unconsolidated silts and very fine sands is
424 0.1 Pa, which corresponds to a $u(x,10-H)$ of ~ 20 cm/s according to Eq. (4), we could see from the result
425 (Fig.12) that sediment resuspension and transport by the ISWs start from the outer shelf already. The observed
426 enhancement of near-bottom (10 m above seafloor) SPM concentration above the outer shelf and the seaward
427 margin of the MDC (Fig. 2) provides evidence for active transport there. Pulses of shoreward transport become
428 increasingly prominent after passing through the critical point at 9.21°W and reach their maxima at the potential
429 breaking point, which is located at the inner part of the MDC.
430 Our simulation results indicate significant differences in the transformation of the ISWs in three periods
431 (pre-, intra- and post-storm) due to a variation of the density field (Fig. 12). In the post-storm period, the initial
432 internal wave remains in a soliton-like shape until reaching the shelf edge, and transforms into a dispersive wave
433 packet afterwards. Intensification of the horizontal velocity associated with the ISWs occurs from the outer shelf
434 till the seaward edge of the MDC, and is strong enough to induce resuspension of local unconsolidated fine-
435 grained sediment (from silts to fine sands).
436 **5. Discussion**

437 **5.1. Implication of simulation results**

438 Through a combination of field data analysis and numerical modeling we investigated the potential impact of
439 mode-1 internal solitary waves on sediment remobilization and transport across a mid-shelf mud depocenter on
440 the NW Iberian shelf. The meteorological and oceanographic conditions used in the study are associated with a
441 downwelling-inducing storm that was representative for the typical extreme winter climate in the NE Atlantic

(Vitorino et al., 2002). Although our internal wave model is based on the weakly nonlinear theory, which falls short in reproducing nonlinear internal waves to the full extent (e.g. breaking and subsequent vortices), a good agreement between simulation results and field data was obtained. Hence, the model is robust in capturing the essential features of the internal solitary waves during their shoaling from the shelf edge to shallow coastal water before potential breaking. The general validity of eKdV models in capturing the characteristics of large amplitude ISWs in coastal oceans has also been demonstrated in other studies, for example in a review by Helfrich and Meiville (2006). The modeled large amplitude ISWs in our study have periods of 750-1600 s before their potential breaking, close to the observed periods of high-frequency wave pulses (1000-1400 s, Fig. 2, 3 and 4) at the lander. It is worth to note that these high-frequency internal waves observed above the lander site should not be breaking-induced vortices. This is because that the latter shall have a frequency close to the local buoyancy frequency N (e.g. Antenucci and Imberger, 2001; Van Haren 2009; Walter et al., 2012; Masunaga et al., 2015). The observed near-bottom (10 m above seafloor) buoyancy frequency N was around 2×10^{-3} s^{-1} (= 500 s in period) and 7×10^{-3} s^{-1} (=143 s in period) at the outer (Station 37) and the inner margin (Station 38) of the MDC in the post-storm period, respectively (Fig. 2). Although a peak centered at ~450 s is shown in the energy spectra (Fig. 5), it is not significant enough. Therefore we are confident to believe that our model successfully reproduced the observed unbroken internal waves above the nucleus of the MDC.

5.1.1. Relationship between internal waves and sediment transport

It is particularly worth mentioning that the onset of increasing SPM concentration (00:00 UTC on 22 September) at the lander occurred immediately after the first group of enhanced internal waves passed (Fig. 4c and 4d). The analysis of field observations in section 4.1.3 indicates that this enhanced level of SPM concentration was attributed to an internal wave-induced persistent sediment transport from the margin toward the nucleus of the MDC. Simulation results (section 4.2) further suggest that a major part of the SPM originates from the seaward margin of the MDC. It is seen from Fig. 12 that the horizontal current associated with the ISWs was enhanced at the outer shelf in the post-storm period. On the other hand, the lander observation indicates shoreward and relatively weak currents (< 2 cm/s) appeared within a few meters above the seafloor after strong offshore-directed internal wave motions and lasted considerably long (Fig. 3e). This implies that sediment resuspended by the enhanced internal waves would be partly transported onshore toward the MDC, which is

469 further proved by the net onshore transport at the lander site (Fig. 6)..

470 The time needed to transport the resuspended sediment from the outer shelf to the lander may explain the
471 time lag between the observed maxima of current velocity and SPM concentration (Fig. 4). Similar phenomena
472 showing coexistence of elevated SPM level and weak current near the seafloor has been observed also in other
473 areas and attributed to enhanced bottom shear stress induced by upstream propagating leading ISWs (e.g. Bogucki
474 et al., 1997; Cheriton et al., 2014).

475 **5.1.2. Storm impact on internal waves and MDC**

476 A particularly striking finding of our study concerns the impact of a deepened pycnocline caused by the
477 storm-induced downwelling on the shoaling and transformation of internal waves, which subsequently affected
478 sediment dynamics across the MDC. It has been recognized that the interaction between internal waves and
479 MDCs is episodic and dependent upon water stratification, with a notable effect under certain circumstances such
480 as upwelling and downwelling conditions when stratification close to the depth of the MDCs is enhanced
481 (Cheriton et al., 2014). Our results provide evidence for this argument. Both model results and field echograms
482 indicate that large amplitude ISWs appeared mostly on the inner shelf where the seafloor was located at depths
483 between 65 and 100 m before the storm (Fig. 7). Also their potential breaking should occur at a similar depth. As
484 a result the mid-shelf seafloor sediment, including the MDC, is only slightly affected by the ISWs (Fig. 12).
485 Under such circumstance a mild transport of SPM is expected on the mid- and outer shelf according to the
486 simulation result (Fig. 12). This scenario might represent non-storm condition for the entire year. During the
487 storm the transformation of the ISWs was significantly altered due to a change in the density field. The potential
488 breaking point of the leading ISW shifted to a deeper location (~106 m) that approaches the inner margin of the
489 MDC (Fig. 12). The initial internal disturbance transforms into a dispersive packet led by a ~30 m-amplitude
490 wave on the outer shelf already (between 9.3° and 9.2°W). This relatively large-amplitude leading wave and its
491 following packet result in an enhancement of the horizontal orbital velocity in both directions, which might have
492 an impact on the near-bottom sediment transport. However, a major part of the MDC remains still unaffected by
493 the change of ISWs during the storm (Fig. 12). The potential breaking point of the leading ISW shifted toward the
494 nucleus of the MDC by ~ 1 km after the storm, reaching a depth of 110 m. The shoaling of the ISWs in the post-
495 storm period resulted in an active sediment resuspension at the seaward margin of the MDC and subsequent

transport in both onshore and offshore directions as described previously. The observed onset of increasing SPM concentration in the post-storm period also suggests that internal wave-induced sediment resuspension above the MDC was not enhanced until the storm passed. Based on these results, we have the confidence to believe that the impact of mode-1 long ISWs on the seafloor sediment is mainly confined at the inner shelf shallower than 100 m before the storm, and the trailing wave packet had the capability to transport resuspended sediment toward the MDC, while during the storm and in the post-storm relaxation period the impact of ISWs on the outer shelf seafloor including the seaward margin of the MDC was gradually enhanced, and resulted in an active sediment resuspension and cross-shelf transport that restricted the offshore extension of the MDC and on the other hand facilitated deposition on the nucleus of the MDC centered around the 120 m isobath.

5.2. Limitation of simulation results

Although our model results are able to reproduce the shoaling of ISWs from the shelf edge to the outer part of the MDC, the effect of a single packet of ISWs alone can neither explain the complicated flow patterns (Fig. 3) nor the near-bottom sediment transport (Fig. 6) observed from the field. A combined effect of low-frequency forcing (e.g. tide, secondary circulation) and high-frequency ISWs should be taken into account. This is clearly shown in the observed current data (Fig. 3). Further contributions come from more energetic ISWs and interaction between different groups of ISWs. As pointed out in the previous section, the initial conditions (amplitude and length) of ISWs have an influence on the amplitude of the leading ISW, the number of each trailing wave and the rate it is generated with. A larger initial internal wave or disturbance would lead to a more developed dispersive wave packet and larger leading waves. Observation data at the lander site do not show a decreasing trend in the wave amplitude which is characteristic of wave packet generated by one single initial disturbance (Fig. 8c). This indicates coexistence of ISWs originated from different sources. Simulation with a larger initial amplitude (40 m) indicates that the leading ISW develops an amplitude of ~85 m when it approaches the seafloor at -118 m before potential breaking, and induces offshore and onshore directed orbital velocities of up to 0.65 and 1 m/s near the seafloor, respectively. A considerably long period (about 1.4 hrs) of offshore-directed current preceding the large amplitude leading wave results in a maximum horizontal dispersal of ~2 km in this scenario, while the subsequent shorter-lasting but stronger onshore current would further enhance sediment resuspension and stretches the SPM plume. These simulation results demonstrate that large amplitude and long ISWs are quite efficient in transporting

resuspended sediment across the shelf. This is also proved by observations in other areas where ISW-induced near-bottom offshore current velocity can reach up to several tens of cm/s and sustain for a few hrs (e.g. Noble and Xu, 2003; Butman et al., 2006). A combined effect of long solitary waves and low-frequency currents would further enhance the transport.

6. Conclusions

Through a combination of field data analysis and numerical modeling we investigated how an energetic winter atmospheric storm in the NE Atlantic modulated the shoaling of mode-1 internal solitary waves on the NW Iberian shelf and its consequence on sediment remobilization and transport across a mid-shelf mud depocenter (110 - 130 m WD). Three major conclusions are drawn from this study. Firstly, mid-shelf mud depocenters are not necessarily areas of permanently calm conditions where fine-grained sediment can settle straightforwardly. They could also result from convergent sediment transport from both onshore and offshore directions. Sediments at both the seaward and the shoreward margins of a mid-shelf mud depocenter may be resuspended by ISWs and subsequently transported across the depocenter itself, particularly during and after downwelling-inducing storms that represent recurrent rough sea conditions.

Secondly, deepening of the pycnocline on the mid- and inner shelf by storm-induced downwelling can lead to a dramatic change of ISWs with a significant impact on sediment dynamics (resuspension, transport and deposition) across mid-shelf mud depocenters. The altered shoaling of the ISWs induced by the storm and enhancement of bottom shear stress at the outer shelf provides a sound explanation for the heterogeneity of the seafloor sediment grain size across the shelf, i.e. a very characteristic gradual coarsening from the nucleus of the mud depocenter in both onshore and offshore directions. The shoreward coarsening of grain size is attributed to a combined effect of surface and internal gravity waves as well as their interaction with coastal currents, while the seaward coarsening can be caused by ISWs alone in the absence of strong currents on the outer shelf, such as the case in our study area.

Finally, an asymmetry in the excursion direction of the ISWs and associated near-bottom processes (e.g. flow reversal and Ekman transport) enables an efficient cross-shelf transport of fine-grained sediment. This asymmetry marks a major difference in the efficiency of near-bottom sediment transport between internal and

surface gravity waves. As shelf mud depocenters are distributed worldwide, our results may also be applicable to other areas, especially those sharing similar oceanographic settings characterized by energetic ISWs.

7. Data availability

All data derived from the cruise (M110) are summarized in the public accessible cruise report through https://www.tib.eu/suchen/id/awi:- doi:10.2312%252Fcr_m110/. Field and model data used in this study can be directly accessed from the online repository at https://github.com/wzhang-hzg/M110. The internal wave model is available at https://lmnad.nntu.ru/en/projects/igwresearch/.

Acknowledgements

We would like to express our special gratitude to Captain Rainer Hammann and his team of RV METEOR. Their great interest, intense support, and high expertise made the challenging GALIMOS cruise (M110) a successful voyage. W. Zhang is supported by the research programme "Marine, Coastal and Polar Systems" (PACES II) of the Hermann von Helmholtz-Gemeinschaft Deutscher Forschungszentren e.V.. The cruise was funded by the DFG Research Center/Excellence Cluster ‘‘The Ocean in the Earth System’’ (EXC309) at the University of Bremen. The study in addition received support from the State Task Programme in the sphere of scientific activity of the Ministry of Education and Science of the Russian Federation (project No. 5.1246.2017/4.6).

References

Antenucci, J. P., Imberger J., 2001. On internal waves near the high-frequency limit in an enclosed basin. Journal of Geophysical Research, 106(C10), 22465–22474. doi:10.1029/2000jc000465

Barton, E. D., Inall, M. E., Sherwin, T. J., Torres, R., 2001. Vertical structure, turbulent mixing and fluxes during Lagrangian observations of an upwelling filament system off Northwest Iberia. Progress in Oceanography 51, 249–267. doi: 10.1016/S0079-6611(01)00069-6

Blair, N. E., Aller, R. C., 2012. The fate of terrestrial organic carbon in the marine environment. Annual Review of Marine Science, 4, 401–423. doi:10.1146/annurev-marine-120709-142717

Boegman, L., Ivey, G. N., 2009. Flow separation and resuspension beneath shoaling nonlinear internal waves. Journal of Geophysical Research, 114, C02018. doi:10.1029/2007jc004411

574 Bogucki, D., Dickey, T., Redekopp, L .G., 1997. Sediment resuspension and mixing by resonantly generated internal solitary
575 waves. Journal of Physical Oceanography, 27, 1181–1196.
576 Bourgault, D., Morsilli, M., Richards, C., Neumeier, U., Kelley, D. E., 2014. Sediment resuspension and nepheloid layers
577 induced by long internal solitary waves shoaling orthogonally on uniform slopes. Continental Shelf Research, 72, 21–33.
578 doi:10.1016/j.csr.2013.10.019
579 Bursik, M., 1995. Theory of the sedimentation of suspended particles from fluvial plumes. Sedimentology, 42(6), 831–838.
580 doi:10.1111/j.1365-3091.1995.tb00412.x
581 Butman, B., Alexander, P. S., Scotti, A., Beardsley, R. C., Anderson, S. P., 2006. Large internal waves in Massachusetts Bay
582 transport sediments offshore. Continental Shelf Research, 26(17–18), 2029–2049. doi:10.1016/j.csr.2006.07.022
583 Cacchione, D. A., Drake, D. E., 1986. Nepheloid layers and internal waves over continental shelves and slopes. Geo-Marine
584 Letters, 6, 147–152. doi:10.1007/bf02238085
585 Cacchione, D. A., Grant, W. D., Drake, D. E., Glenn, S., 1987. Storm-dominated bottom boundary layer dynamics on the
586 northern California continental shelf: Measurements and predictions. Journal of Geophysical Research, 92(C2), 1817–182.
587 doi:10.1029/jc092ic02p01817
588 Cheriton, O. M., McPhee-Shaw, E. E., Shaw, W. J., Stanton, T. P., Bellingham, J. G., Storlazzi, C. D., 2014. Suspended
589 particulate layers and internal waves over the southern Monterey Bay continental shelf: An important control on shelf mud
590 belts ? Journal of Geophysical Research, 119, 428–444. doi:10.1002/2013jc009360
591 da Silva, J. C. B., Ermakov, S. A., Robinson, I. S., Kijash, S. V., 1998. Role of surface films in ERS SAR signatures of internal
592 waves on the shelf 1. Short-period internal waves. Journal of Geophysical Research, 103, 8009–8031. doi:
593 10.1029/2000JC900053
594 Dias, J. M. A., Gonzalez, R., Garcia, C., Diaz-del-Rio, V., 2002. Sediment distribution patterns on the Galicia-Minho
595 continental shelf. Progress in Oceanography, 52, 215–231. doi:10.1016/s0079-6611(02)00007-1
596 Geyer, W. R., Hill, P. S. Kineke, G. C., 2004. The transport, transformation and dispersal of sediment by buoyant coastal
597 flows. Continental Shelf Research, 24, 927–949. doi:10.1016/j.csr.2004.02.006
598 Grimshaw, R., Pelinovsky, E., Talipova, T., Kurkina, O., 2004. Simulation of the transformation of internal solitary waves on
599 oceanic shelves. Journal of Physical Oceanography, 34, 2774–2791. doi:10.1175/jpo2652.1
600 Grimshaw, R., Pelinovsky, E., Talipova, T., Kurkina, O., 2010. Internal solitary waves: propagation, deformation and
601 disintegration. Nonlinear Processes in Geophysics, 17, 633–649. doi:10.5194/npg-17-633-2010
602 Grimshaw, R., Guo, C., Helfrich, K., Vlasenko, V., 2014. Combined effect of rotation and topography on shoaling oceanic
603 internal solitary waves. Journal of Physical Oceanography, 44, 1116–1132. doi:10.1175/jpo-d-13-0194.1

Hale, R. P., Ogston, A. S., 2015. In situ observations of wave-supported fluid-mud generation and deposition on an active continental margin. Journal of Geophysical Research, 120(11), 2357–2373. doi:10.1002/2015jf003630

Hanebuth, T. J. J., Lantzsch, H., Nizou, J., 2015a. Mud depocenters on continental shelves – appearance, initiation times, and growth dynamics. Geo-Marine Letters, 35(6), 487-503. doi:10.1007/s00367-015-0422-6

Hanebuth, T. J. J., Aepfler, R., Diaz, V., Cui, Y., Didenkulova, I., Dolan, A., ... Zhang, W., 2015b. GALIMOS – Monitoring the interaction between Oceanographic elements and Sedimentary seabed structures at the GALIcian margin, RV METEOR cruise M110 GALIMOS, Sept. 15–30, 2014, Vigo (Spain) – Cádiz (Spain). Meteor-Ber., M110, 69 pp. doi:10.2312/cr_m110

Hedges, J. I., Keil, R. G., 1995. Sedimentary organic matter preservation: an assessment and speculative synthesis. Marine Chemistry, 49, 81–115. doi:10.1016/0304-4203(95)00008-f

Helfrich, K. R., Melville, W. K., 2006. Long nonlinear internal waves. Annual Review of Fluid Mechanics, 38(1), 395–425. doi:10.1146/annurev.fluid.38.050304.092129

Hill, P. S., McCave, I. N., 2001. Suspended particle transport in benthic boundary layers, in The Benthic Boundary Layer: Transport Processes and Biogeochemistry, edited by B. P. Boudreau and B. B. Jorgensen, pp. 78–103, Oxford Univ. Press, N. Y.

Holloway, P., Pelinovsky, E., Talipova, T., 1999. A generalized Korteweg–De Vries model of internal tide transformation in the coastal zone. Journal of Geophysical Research, 104(C8), 18333–18350. doi:10.1029/1999jc900144

Hosegood, P., Bonnin, J., van Haren, H., 2004. Solibore-induced sediment resuspension in the Faeroe-Shetland channel. Geophysical Research Letters, 31, L09301. doi:10.1029/2004gl019544

Inthorn, M., Mohrholz, V., Zabel, M., 2006. Nepheloid layer distribution in the Benguela upwelling area offshore Namibia. Deep Sea Research I, 53(8), 1423–1438. doi:10.1016/j.dsr.2006.06.004

Johnson, D. R., Weidemann, A., Pegau, W. S., 2001. Internal tidal bores and bottom nepheloid layers. Continental Shelf Research, 21,1473–1484. doi:10.1016/s0278-4343(00)00109-6

Korteweg, D. J., de Vries, G., 1895. On the change of form of long waves advancing in a rectangular canal, and on a new type of long stationary waves. Philosophical Magazine, 39(240), 422–443. doi:10.1080/14786449508620739

Kurkina, O. E., Kurkin, A. A., Pelinovsky, E. N., Semin, S. V., Talipova, T. G., Churaev, E. N., 2016. Structure of currents in the soliton of an internal wave. Oceanology, 56(6), 767–773.

Lamb, K. G., 2014. Internal wave breaking and dissipation mechanisms on the continental slope/shelf. Annual Review of Fluid Mechanics 46, 231–254.

Magalhaes, J. M., da Silva, J. C. B., 2012. SAR observations of internal solitary waves generated at the Estremadura Promontory off the west Iberian coast. Deep-Sea Research I, 69, 12–24. doi:10.1016/j.dsr.2012.06.002

Mahiques, M. M., Hanebuth, T. J. J., Martins, C. C., Montoya-Montes, I., Alcántara-Carrío, J., Figueria, R. C. L., Bícego, M. C., 2016. Mud depocenters on the continental shelf – a neglected sink for anthropogenic contaminants released in the coastal zone. Environmental Earth Sciences, 75, 44–55. doi:10.1007/s12665-015-4782-z

Masunaga, E., Homma, H., Yamazaki, H., Fringer, O. B., Nagai, T., Kitade, Y., Okayasu, A., 2015. Mixing and sediment resuspension associated with internal bores in a shallow bay. Continental Shelf Research, 110, 85–99. doi:10.1016/j.csr.2015.09.022

McCave, I. N., 1973. Transport and escape of fine-grained sediment from shelf areas, in Shelf sediment transport: process and pattern, edited by D. J. P. Swift, D. B. Duane, and O. H. Pilkey, pp. 225–244, Dowden, Hutchinson Ross, Stroudsburg, pa.

McCave, I. N., Hall, I. R., Antia, A. N., Chou, L., Dehairs, F., Lampitt, R. S., Thomsen, L., van Weering, T. C. E. Wollast, R., 2001. Distribution, composition and flux of particulate material over the European margin at 47°–50°N. Deep Sea Research, Part II: Topical Studies in Oceanography, 48, 3107–3139. doi: 10.1016/s0967-0645(01)00034-0

McKee, B. A., Aller, R. C., Allison, M. A., Bianchi, T. S. Kineke, G. C., 2004. Transport and transformation of dissolved and particulate materials on continental margins influenced by major rivers: Benthic boundary layer and seabed processes. Continental Shelf Research, 24(7–8), 899–926. doi:10.1016/j.csr.2004.02.009

McPhee-Shaw, E. E., Sternberg, R. W., Mullenbach, B., Ogston, A. S., 2004. Observations of intermediate nepheloid layers on the northern California continental margin. Continental Shelf Research, 24, 693–720. doi:10.1016/j.csr.2004.01.004

Morsilli, M., Pomar, L., 2012. Internal waves vs. surface storm waves: a review on the origin of hummocky cross-stratification. Terra Nova, 24(4), 273–282. doi:10.1111/j.1365-3121.2012.01070.x

Moum, J. N., Smyth, W. D., 2006. The pressure disturbance of a nonlinear internal wave train. Journal of Fluid Mechanics 558, 153–177.

Noble, M. A., Xu, J. P., 2003. Observations of large-amplitude cross-shore internal bores near the shelf break, Santa Monica Bay, CA. Marine Environmental Research, 56, 127–149. doi:10.1016/s0141-1136(02)00328-8

O'Driscoll, K., Levine, M., 2017. Simulations and observation of nonlinear internal waves on the continental shelf: Korteweg-de Vries and extended Korteweg-de Vries solutions. Ocean Science 13, 749–763.

Ogston, A. S., Cacchione, D. A., Sternberg, R. W., Kineke, G. C., 2000. Observations of storm and river flood-driven sediment transport on the Northern California continental shelf. Continental Shelf Research, 20(16), 2141–2162. doi:10.1016/s0278-4343(00)00065-0

Ospina-Alvarez, N., Prego, R., Alvarez, I., de Castro, M., Alvarez-Ossorio, M. T., Pazos, Y., Campos, M. J., . . . Varela, M., 2010. Oceanographical patterns during a summer upwelling–downwelling event in the Northern Galician Rias: comparison

663 with the whole Ria system (NW of Iberian Peninsula). Continental Shelf Research, 30, 1362–1372. doi:
664 10.1016/j.csr.2010.04.018
665 Oliveira, A., Vitorino, J., Rodrigues, A., Jouanneau, J. M., Dias, J. A. Weber, O., 2002. Nepheloid layer dynamics in the
666 northern Portuguese shelf. Progress in Oceanography, 52, 195–213. doi:10.1016/s0079-6611(02)00006-x
667 Palanques, A., Biscaye, P. E., 1992. Patterns and controls of the suspended matter distribution over the shelf and upper slope
668 south of New England. Continental Shelf Research, 12, 557–600. doi:10.1016/0278-4343(92)90021-b
669 Pomar, L., Morsilli, M., Hallock, P., Bádenas, B., 2012. Internal waves, an under-explored source of turbulence events in the
670 sedimentary record. Earth Science Reviews, 111(1–2), 56–81. doi:10.1016/j.earscirev.2011.12.005
671 PO-WAVES Group, 1994. Final report of sub-project A, Wind wave climatology of the Portuguese coast, Instituto Hidrografico,
672 REL. FT. OM 5/94, 106 pp.
673 Quaresma, L. S., Vitorino, J., Oliveira, A., da Silva, J., 2007. Evidence of sediment resuspension by nonlinear internal waves
674 on the western Portuguese mid-shelf. Marine Geology, 246, 123–143. doi:10.1016/j.margeo.2007.04.019
675 Richards, C. G., Bourgault, D., Galbraith, P. S., Hay, A., Kelley, D. E., 2013. Measurements of shoaling internal waves and
676 turbulence in an estuary. Journal of Geophysical Research, 118(1), 1–14. doi:10.1029/2012jc008154
677 Relvas, P., Barton, E. D., Dubert, J., Oliveira, P. B., Peliz, A., da Silva, J. C. B., Santos A. M. P., 2007. Physical oceanography
678 of the western Iberia ecosystem: latest views and challenges. Progress in Oceanography, 74(2–3), 149–173.
679 doi:10.1016/j.pocean.2007.04.021
680 Shanmugam, G., 2013. Modern internal waves and internal tides along oceanic pycnoclines: Challenges and implifications for
681 ancient deep-marine baroclinic sands. AAPG Bulletin, 97(5): 799–843. doi:10.1306/10171212101
682 Syvitski, J. P., Morehead, M. D., 1999. Estimating river-sediment discharge to the ocean: Application to the Eel margin,
683 northern California. Marine Geology, 154, 13–28. doi:10.1016/s0025-3227(98)00100-5
684 Talipova, T., Pelinovsky, E., Kurkin, A., Kurkina, O., 2014. Modeling the dynamics of intense internal waves on the shelf.
685 Izvestiya, Atmospheric and Ocean Physics, 50(6), 630–637. doi:10.1134/s0001433814060164
686 Traykovski, P., Geyer, W. R., Irish, J. D., Lynch, J. F., 2000. The role of wave-induced density-driven fluid mud flows for
687 cross-shelf transport on the Eel River continental shelf. Continental Shelf Research, 20(16), 2113–2140. doi:10.1016/s0278-
688 4343(00)00071-6
689 Traykovski, P., Wiberg, P. L., Geyer, W. R., 2007. Observations and modeling of wave-supported sediment gravity flows on
690 the Po pro-delta and comparison to prior observations from the Eel shelf. Continental Shelf Research, 27, 375–399.
691 doi:10.1016/j.csr.2005.07.008

692 Van Haren, H., 2009. Using high sampling-rate ADCP for observing vigorous processes above sloping (deep) ocean bottoms.
693 Journal of Marine Systems, 77, 418–427. doi:10.1016/j.jmarsys.2008.10.012
694 Van Haren, Puig, P., 2017. Internal wave turbulence in the Llobregat prodelta (NW Mediterranean) under stratified conditions:
695 A mechanism for sediment waves generation? Marine Geology, 388, 1-11. doi: 10.1016/j.margeo.2017.04.008
696 Varela, R. A., Roson, G., Herrera, J. L., Torres-Lopez, S., Fernandez-Romero, A., 2005. A general view of the hydrographic
697 and dynamical patterns of the Rias Baixas adjacent sea area. Journal of Marine Systems, 54, 97–113. doi:
698 10.1016/j.jmarsys.2004.07.006
699 Vitorino, J., Oliveira, A., Jouanneau, J. M., Drago, T., 2002. Winter dynamics on the northern Portuguese shelf. Part 1: physical
700 processes. Progress in Oceanography, 52(2), 129–153. doi:10.1016/s0079-6611(02)00003-4
701 Vlasenko, V., Hutter, K., 2002. Numerical experiments on the breaking of solitary internal waves over a slope-shelf topography.
702 Journal of Physical Oceanography, 32(6), 1779–1793.
703 Walsh, J. P., Nittrouer, C. A., 2009. Understanding fine-grained river-sediment dispersal on continental margins. Marine
704 Geology, 263(1–4), 34–45. doi:10.1016/j.margeo.2009.03.016
705 Walter, R. K., Woodson, C. B., Arthur, R. S., Fringer, O. B., Monismith, S. G., 2012. Nearshore internal bores and turbulent
706 mixing in southern Monterey Bay. Journal of Geophysical Research, 117, C07017. doi:10.1029/2012jc008115
707 Wooster, W. S., A. Bakun, D. R. Mclain, 1976. Seasonal upwelling cycle along eastern boundary of North-Atlantic, Journal of
708 Marine Research 34 (2), 131–141.
709 Wright, L. D., Friedrichs, C. T., 2006. Gravity-driven sediment transport on continental shelves: A status report, Continental
710 Shelf Research, 26, 2092–2107. doi:10.1016/j.csr.2006.07.008
711 Wu, J., Ren, J., Liu, H., Qiu, C., Cui, Y., Zhang, Q., 2016. Trapping and escaping processes of Yangtze River-derived sediments
712 to the East China Sea. Geological Society, London, Special Publications, 429(1), 153–169. doi:10.1144/sp429.7
713 Yuan, C., Grimshaw, R., Johnson, E., Chen, X., 2018. The propagation of internal solitary waves over variable topography in
714 a horizontally two-dimensional framework. Journal of Physical Oceanography 48, 283–300.
715 Zhang, W., Cui, Y., Santos, A. I. Hanebuth, T. J. J., 2016. Storm-driven bottom sediment transport on a high-energy narrow
716 shelf (NW Iberia) and development of mud depocenters. Journal of Geophysical Research: Oceans, 121, 5751–5772.
717 doi:10.1002/2015jc011526

718
719
720
721
722

723 **Figure Captions:**

Figure 1. (a) Location of the study area. (b) Bathymetry of the study area delineated by depth contour lines at 20 m intervals on the shelf (< 200 m WD) and color-filled contours (1000 and 2000 m, respectively) off the shelf edge. Nuclei of the MDCs where the mud content exceeds 80% are marked by closed solid curves in red. A sketch map of the M110 GALIMOS cruise showing the 1) cross-shelf track lines with multi-beam (12 kHz) and sediment echo-sounding (18 kHz) data, 2) lander deployment sites (solid triangles), and 3) CTD stations (solid circles marked by numbers) that are relevant to this study is also embedded. (c) Distribution of surface sediment median grain size in the study area. Mud depocenters are delineated by the dashed line (mud content >30%) and the solid line (mud content >80%). This map is modified from Dias et al. (2002).

Figure 2. Cross-shelf density fields revealed by 3D modeling (contour maps) and field measurements (CTD stations) along two neighbouring track lines off the Ría de Vigo (location in Fig. 1) during intra- and post-storm periods, respectively. Note that each CTD profiling terminates at ~9 m above the seafloor and the sampling sequence goes from the shelf edge to the inner shelf. Vertical profiles of SPM concentration, calibrated by water samples *in situ*, are also shown at each station.

Figure 3. Recorded time series of (a) near-bottom (20 cm above seafloor) water density and temperature, (b) surface water level, (c) cross-shelf component (u) of 600 s average current, (d) along-shelf component (v) of 600 s average current, and (e) three selected time slices of u during the post-storm period. These time slices are also marked in (c). Positive values in u and v indicate eastward and northward directions, respectively. Position of the lander is indicated in Fig. 1.

Figure 4. Time series of near-bottom current and SPM recorded by the lander. (a) The cross-shelf component (u) of the current data recorded by the ECM placed 150 cm above the seafloor. (b) The along-shelf component (v) of the current data detected from the same device. (c) The absolute velocity of the current data. The mass concentration and grain size composition of SPM at 30 cm above the seafloor are shown in (d) and (e), respectively. The SPM data were recorded by the LISST100 and calibrated against sediment samples *in situ*. The curve of water level is embedded in (a), (b) and (c) for better interpretation of the data. Three time slices with strong high-frequency oscillations are marked by coloured columns and numbers in (a). Energy spectra for these time slices are plotted in Fig. 4.

Figure 5. (a, b, c) Energy spectra of the cross-shelf component of the bottom current for three selected time slices with strong high-frequency oscillations as indicated in Figure 2 and 3. (d) Power spectral density of the seafloor pressure recorded by the lander for the first time slice. (e, f) Power spectral density of the near-bottom turbidity recorded by ECM for the first two time slices. The spectral resolution is 1.15×10^{-4} Hz. The 95 % confident intervals are shown.

Figure 6. Near-bottom (30 cm above seafloor) sediment transport flux induced by enhanced internal waves in three time slices.

Figure 7. Echograms (18k Hz) along different cross-shelf track lines (see Figure.1 for location) showing different types of internal wave-like reflectors. The abnormal high backscatter signal shown in profile S2 in between 120 and 180 m WD, which is not shown in any other track line, is likely consisted of resuspended SPM originated from actions of internal waves on the outer and mid-shelf seafloor in the post-storm period. . The core of the plume, characterized by highest backscatter intensity, is indicated by the circle.

Figure 8. (a) Density field that integrates the modeled vertical displacement of the pycnocline (η) along S1 during the storm. This figure shows the result for 11 h after the initial disturbance at the open boundary. (b) Echogram (18k Hz) along the same profile derived on the same day. (c) Comparison between field data and model result for the internal waves in the post-storm period. Note that the time for the model result is displayed in a shifted coordinate for a better comparison with field data. The ECM data has a frequency of 4 Hz and the ADCP data is 600 s averaged. Fifth-order band-pass Butterworth filtering is applied to derive the internal wave series from the ECM data.

Figure 9. Initial and final stage of simulated ISW across Profile S1 during the pre-storm (a) and post-storm (b) periods, respectively. Note that the time for the final stage is displayed in a shifted coordinate for a better comparison with the initial condition.

Figure 10. Spatial variation of coefficients of the 2DV model along Profile S1 in the post-storm period. The background density field is shown in the bottom panel. Note that the model domain starts from the continental slope (1000 m WD), which is not shown here for better representation of the mid-shelf. Model computation terminates at the place where high order nonlinearity (i.e. the quadratic and cubic nonlinear terms) takes control and the weakly nonlinear assumption is no longer valid. The pycnocline, where $\phi(z)$ reaches its maximum, is marked by the dashed line.

Figure 11. (a) Evolution of a periodic ISW (initial amplitude = 15 m) along Profile S1 in the post-storm period. (b) Near-bottom horizontal orbital velocity $u(x,10-H)$ associated with the ISW. Positive values indicate shoreward direction. (c) Topography of the shelf along Profile S1.

Figure 12. Exceedance probability of the near-bottom horizontal orbital velocity $u(x,10-H)$ associated with propagation of periodic ISW (initial amplitude = 15 m) along Profile S1 in three representative periods (pre-, intra- and post-storm), respectively. The threshold in the strength of $u(x,10-H)$ for resuspension of unconsolidated silt is marked by dashed lines. Note that the plots terminate at the point where high order nonlinearity starts to dominate the transformation of the leading ISW.

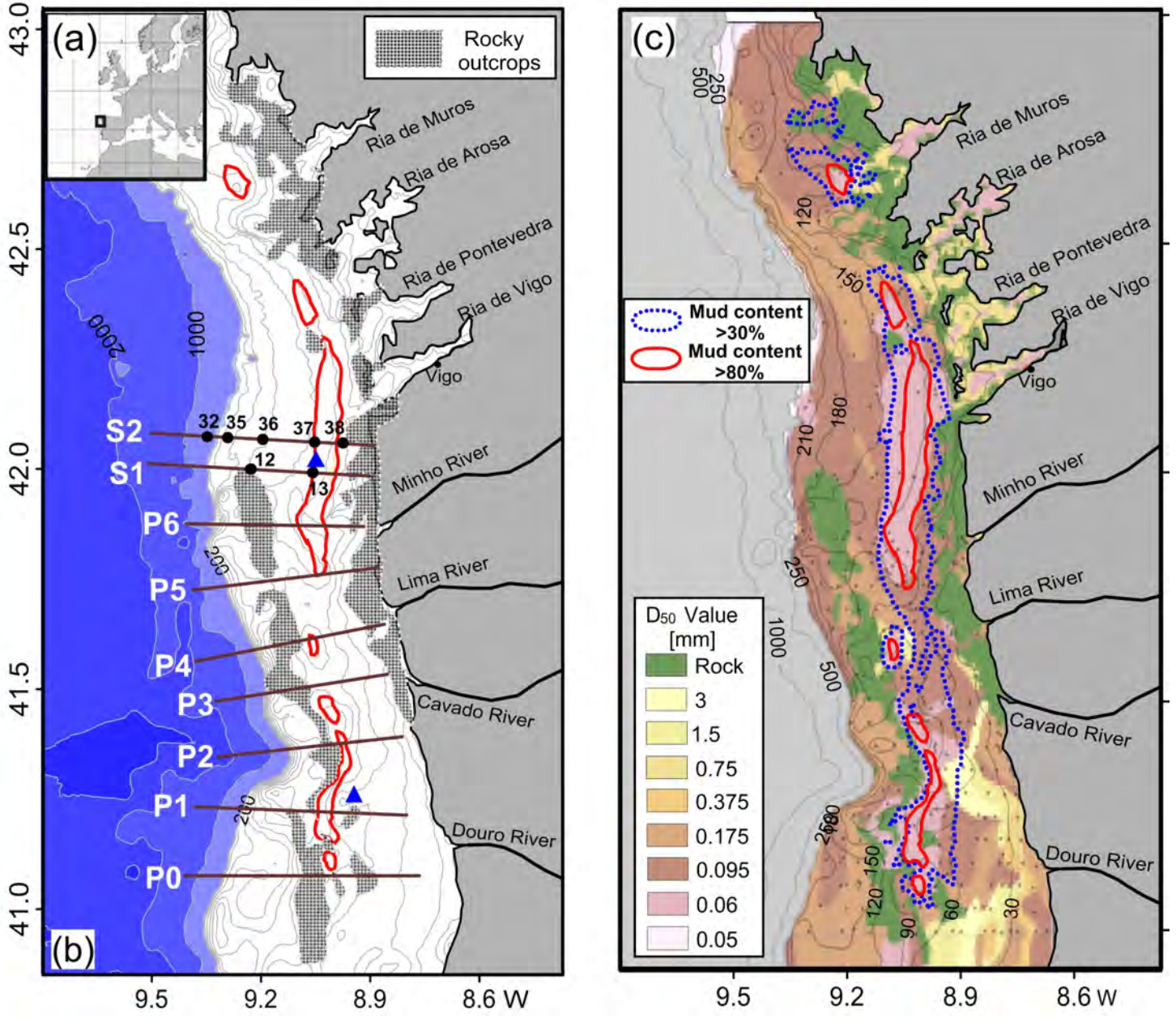
(a)
Rocky outcrops
Ria de Muros
Ria de Arosa
Ria de Pontevedra
Ria de Vigo
Vigo
Minho River
Lima River
Cavado River
Douro River
S2
S1
P6
P5
P4
P3
P2
P1
P0
32
35
36
37
38
12
13
2000
1000
200
(b)
43.0
42.5
42.0
41.5
41.0
9.5
9.2
8.9
8.6 W
(c)
Mud content >30%
Mud content >80%
D50 Value [mm]
Rock
3
1.5
0.75
0.375
0.175
0.095
0.06
0.05
500
250
120
150
180
210
1000
500
250
200
150
120
90
60
30

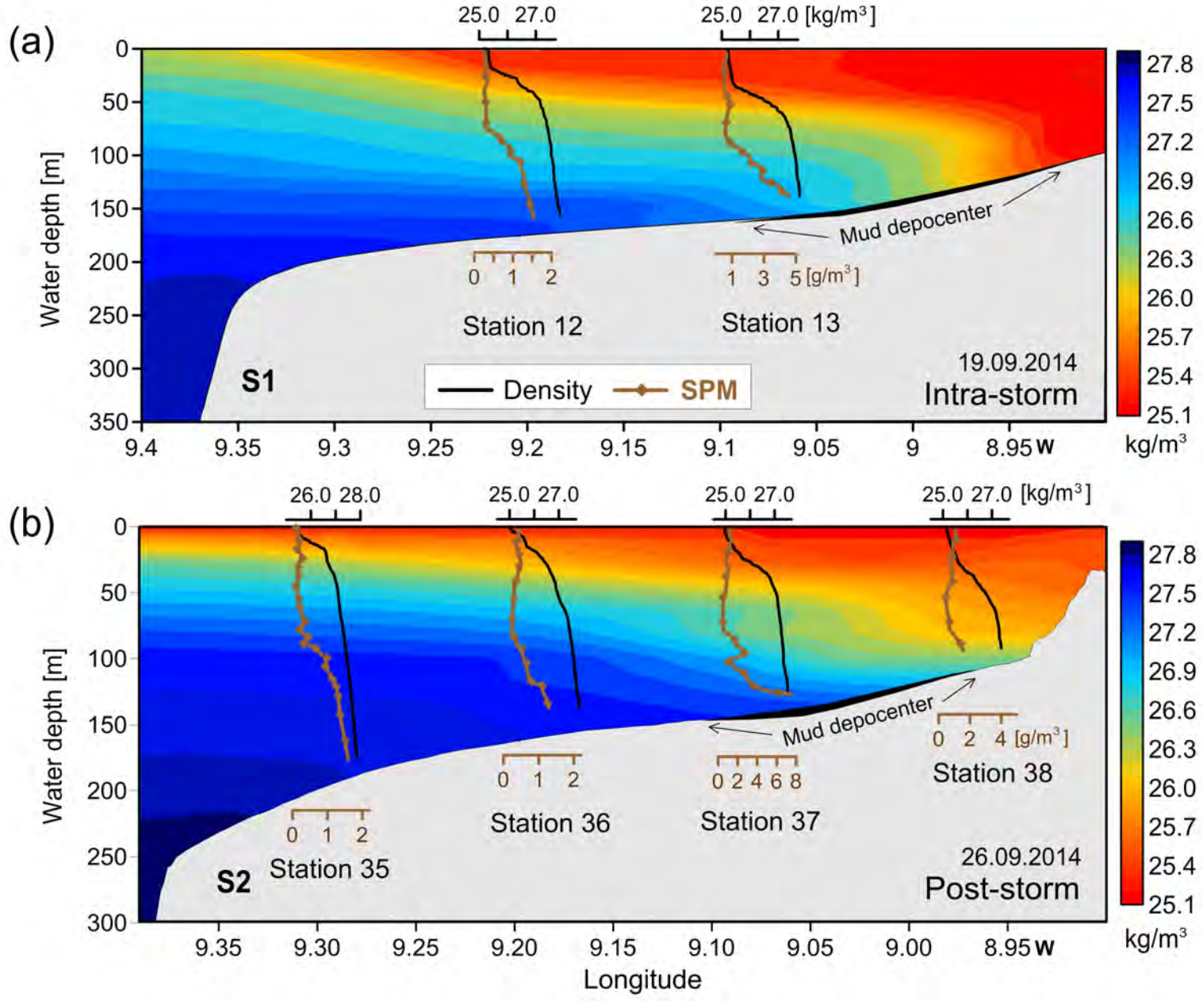
(a)
25.0 27.0
25.0 27.0 [kg/m³]
Water depth [m]
0
50
100
150
200
250
300
350
Mud depocenter
0 1 2
1 3 5 [g/m³]
Station 12
Station 13
S1
Density
SPM
19.09.2014
Intra-storm
9.4 9.35 9.3 9.25 9.2 9.15 9.1 9.05 9 8.95 W
27.8
27.5
27.2
26.9
26.6
26.3
26.0
25.7
25.4
25.1
kg/m³
(b)
26.0 28.0
25.0 27.0
25.0 27.0
25.0 27.0 [kg/m³]
Water depth [m]
0
50
100
150
200
250
300
Mud depocenter
0 2 4 [g/m³]
Station 38
0 1 2
Station 36
0 2 4 6 8
Station 37
0 1 2
Station 35
S2
26.09.2014
Post-storm
9.35 9.30 9.25 9.20 9.15 9.10 9.05 9.00 8.95 W
Longitude
27.8
27.5
27.2
26.9
26.6
26.3
26.0
25.7
25.4
25.1
kg/m³

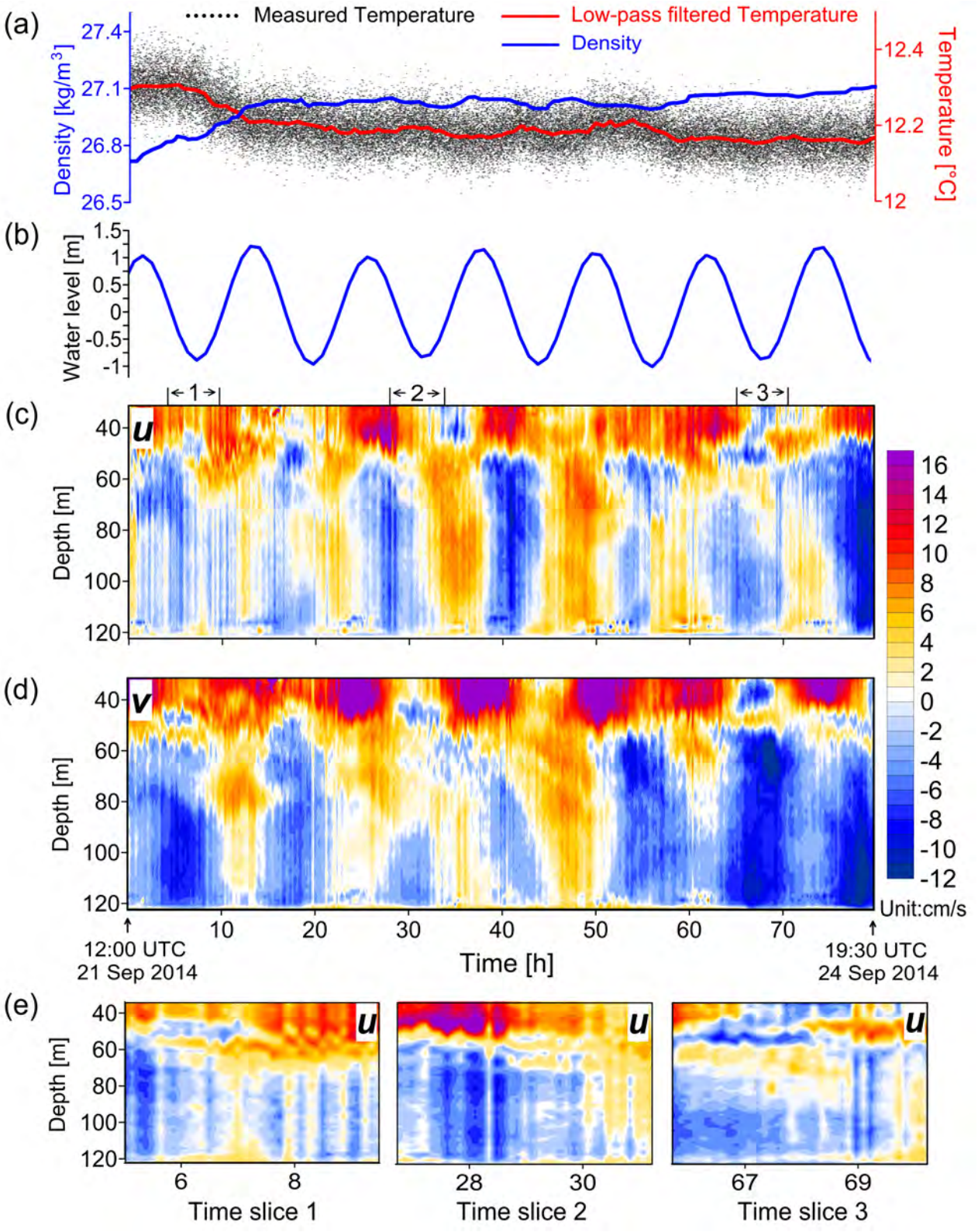
(a)
Measured Temperature
Low-pass filtered Temperature
Density
Density [kg/m3]
Temperature [°C]
(b)
Water level [m]
(c)
u
Depth [m]
(d)
v
Depth [m]
Unit:cm/s
Time [h]
12:00 UTC
21 Sep 2014
19:30 UTC
24 Sep 2014
(e)
u
Depth [m]
Time slice 1
Time slice 2
Time slice 3

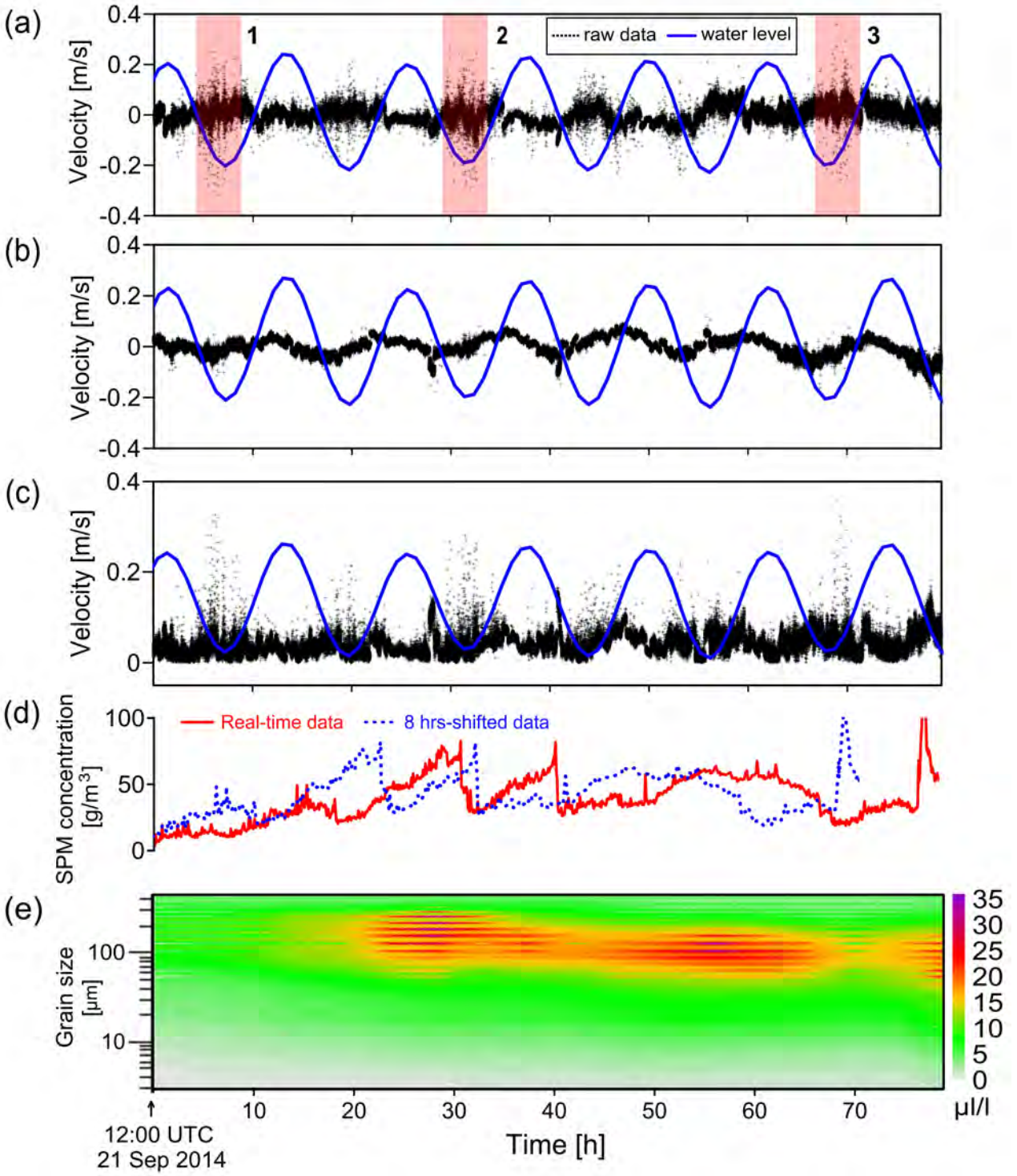
(a)
Velocity [m/s]
0.4
0.2
0
-0.2
-0.4
1
2
3
raw data
water level
(b)
Velocity [m/s]
(c)
Velocity [m/s]
(d)
SPM concentration [g/m³]
100
50
0
Real-time data
8 hrs-shifted data
(e)
Grain size [µm]
100
10
35
30
25
20
15
10
5
0
µl/l
10
20
30
40
50
60
70
12:00 UTC
21 Sep 2014
Time [h]

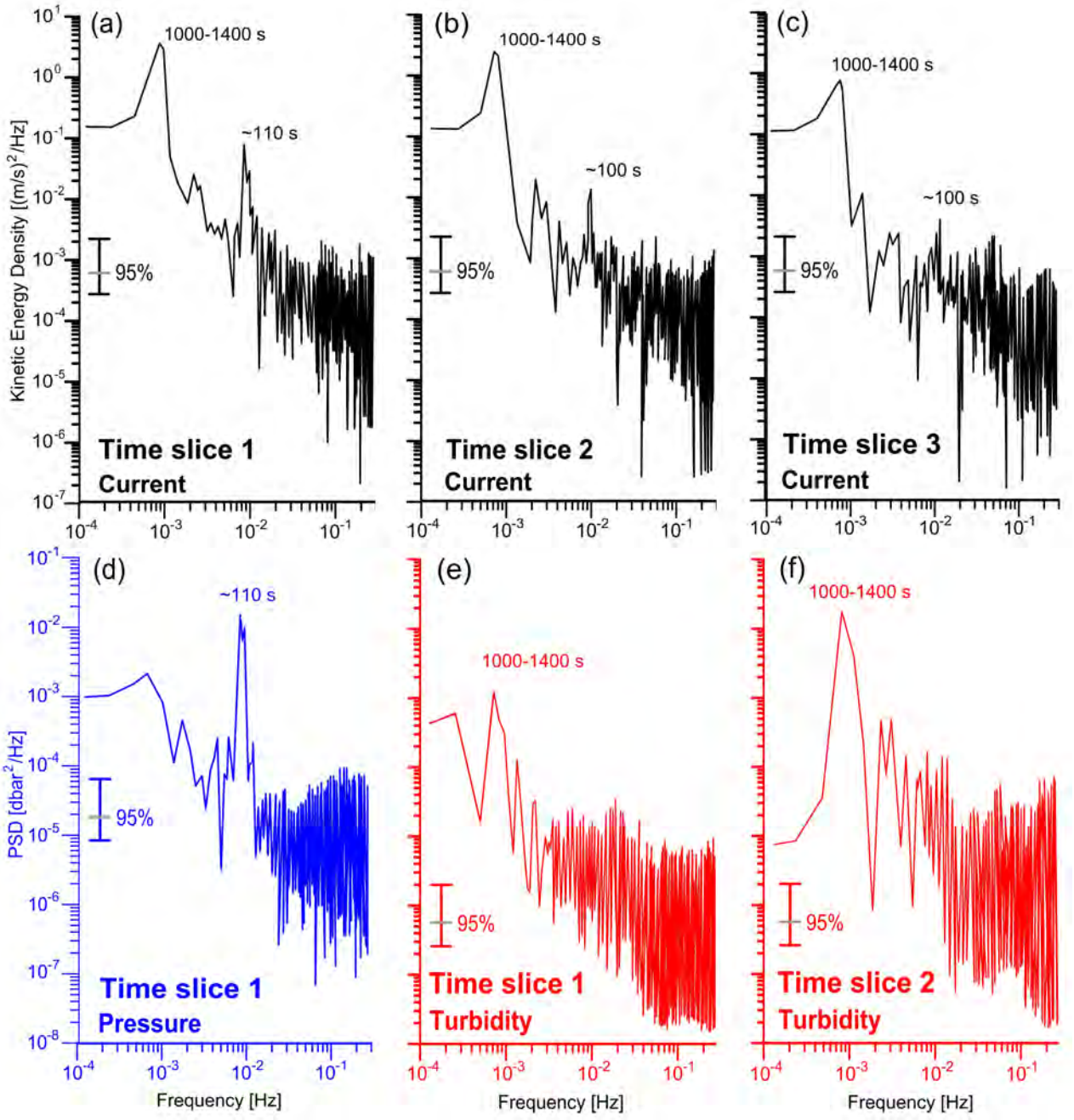
(a)
1000-1400 s
~110 s
95%
Time slice 1
Current
Kinetic Energy Density [(m/s)^2/Hz]
(b)
1000-1400 s
~100 s
95%
Time slice 2
Current
(c)
1000-1400 s
~100 s
95%
Time slice 3
Current
(d)
~110 s
95%
Time slice 1
Pressure
PSD [dbar^2/Hz]
Frequency [Hz]
(e)
1000-1400 s
95%
Time slice 1
Turbidity
Frequency [Hz]
(f)
1000-1400 s
95%
Time slice 2
Turbidity
Frequency [Hz]

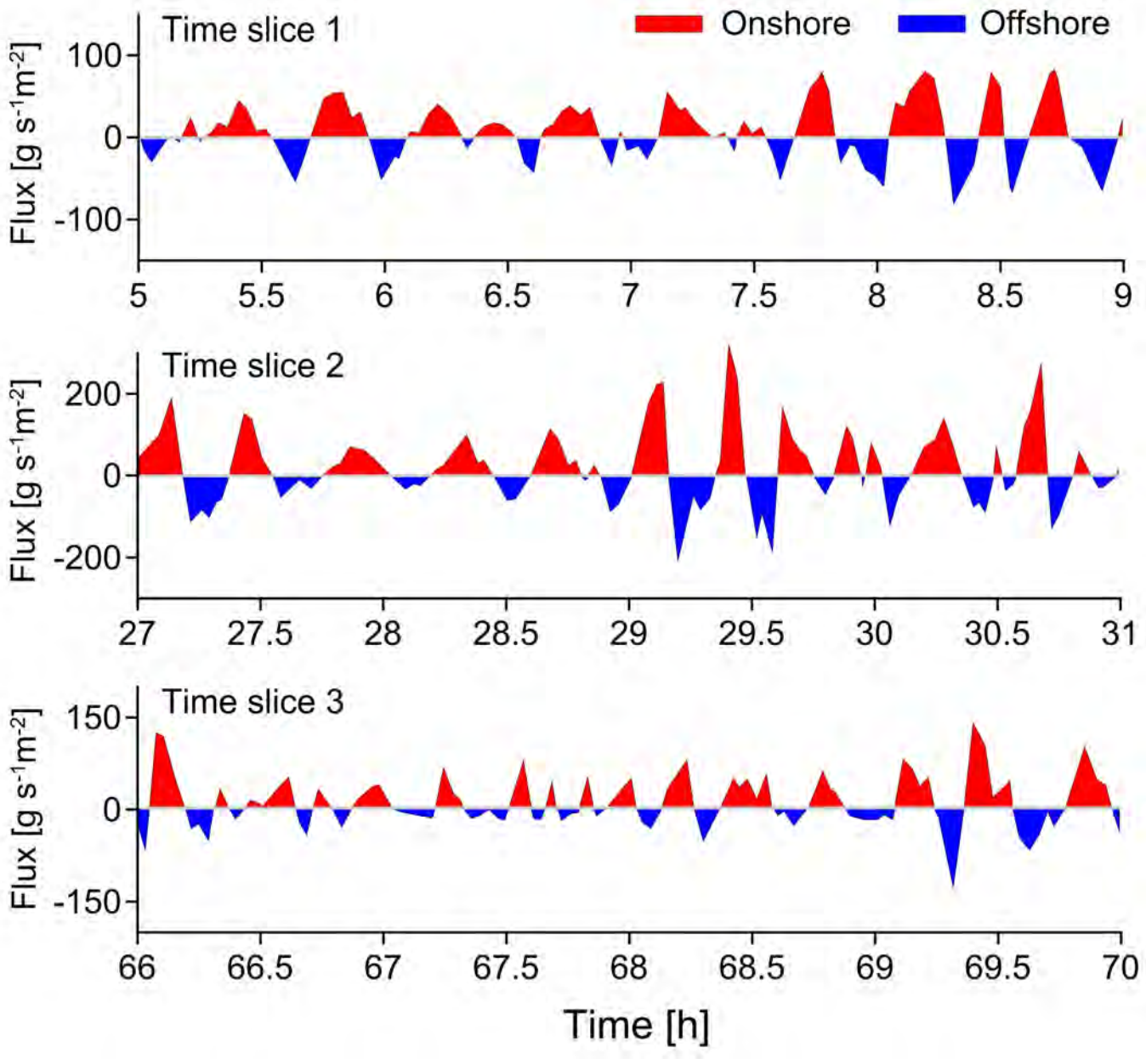
Time slice 1
Onshore
Offshore
Flux [g s-1m-2]
100
0
-100
5
5.5
6
6.5
7
7.5
8
8.5
9
Time slice 2
Flux [g s-1m-2]
200
0
-200
27
27.5
28
28.5
29
29.5
30
30.5
31
Time slice 3
Flux [g s-1m-2]
150
0
-150
66
66.5
67
67.5
68
68.5
69
69.5
70
Time [h]

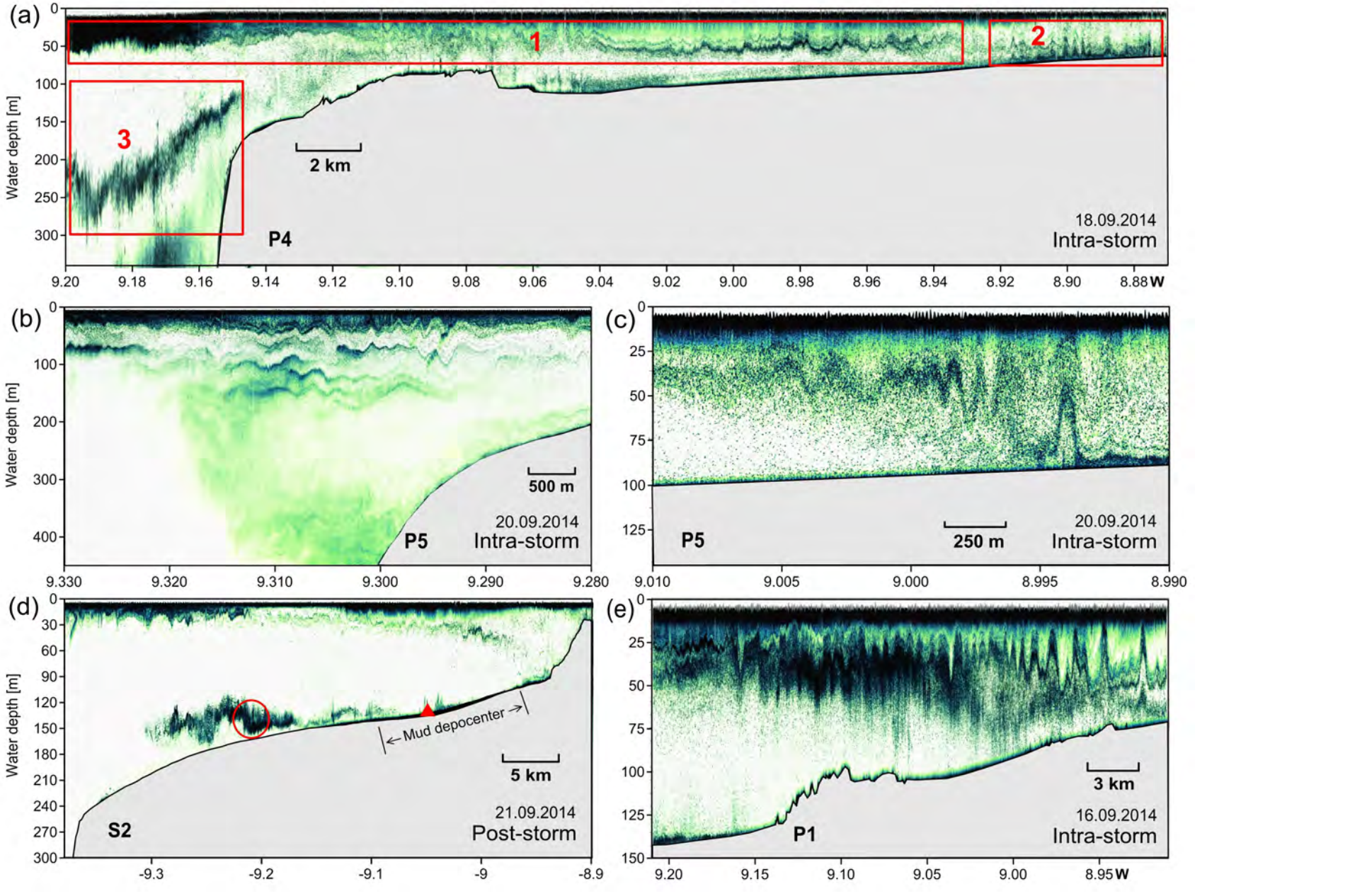
(a)
1
2
3
Water depth [m]
2 km
P4
18.09.2014
Intra-storm
9.20 9.18 9.16 9.14 9.12 9.10 9.08 9.06 9.04 9.02 9.00 8.98 8.96 8.94 8.92 8.90 8.88 W
(b)
Water depth [m]
500 m
P5
20.09.2014
Intra-storm
9.330 9.320 9.310 9.300 9.290 9.280
(c)
P5
250 m
20.09.2014
Intra-storm
9.010 9.005 9.000 8.995 8.990
(d)
Water depth [m]
Mud depocenter
5 km
S2
21.09.2014
Post-storm
-9.3 -9.2 -9.1 -9 -8.9
(e)
3 km
P1
16.09.2014
Intra-storm
9.20 9.15 9.10 9.05 9.00 8.95 W

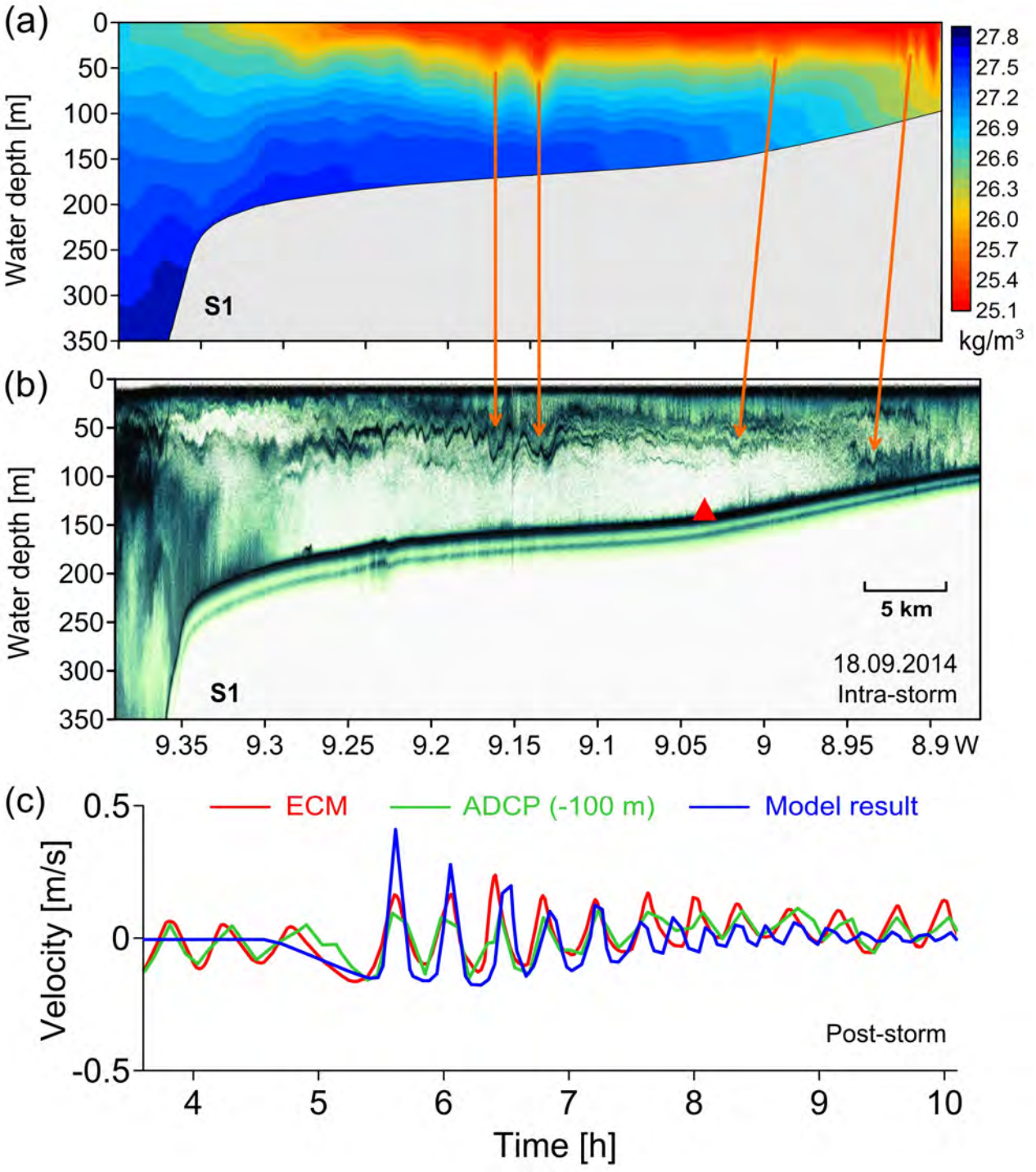
(a)
Water depth [m]
0
50
100
150
200
250
300
350
S1
27.8
27.5
27.2
26.9
26.6
26.3
26.0
25.7
25.4
25.1
kg/m3
(b)
Water depth [m]
S1
5 km
18.09.2014
Intra-storm
9.35
9.3
9.25
9.2
9.15
9.1
9.05
9
8.95
8.9 W
(c)
ECM
ADCP (-100 m)
Model result
Velocity [m/s]
0.5
0
-0.5
Post-storm
4
5
6
7
8
9
10
Time [h]

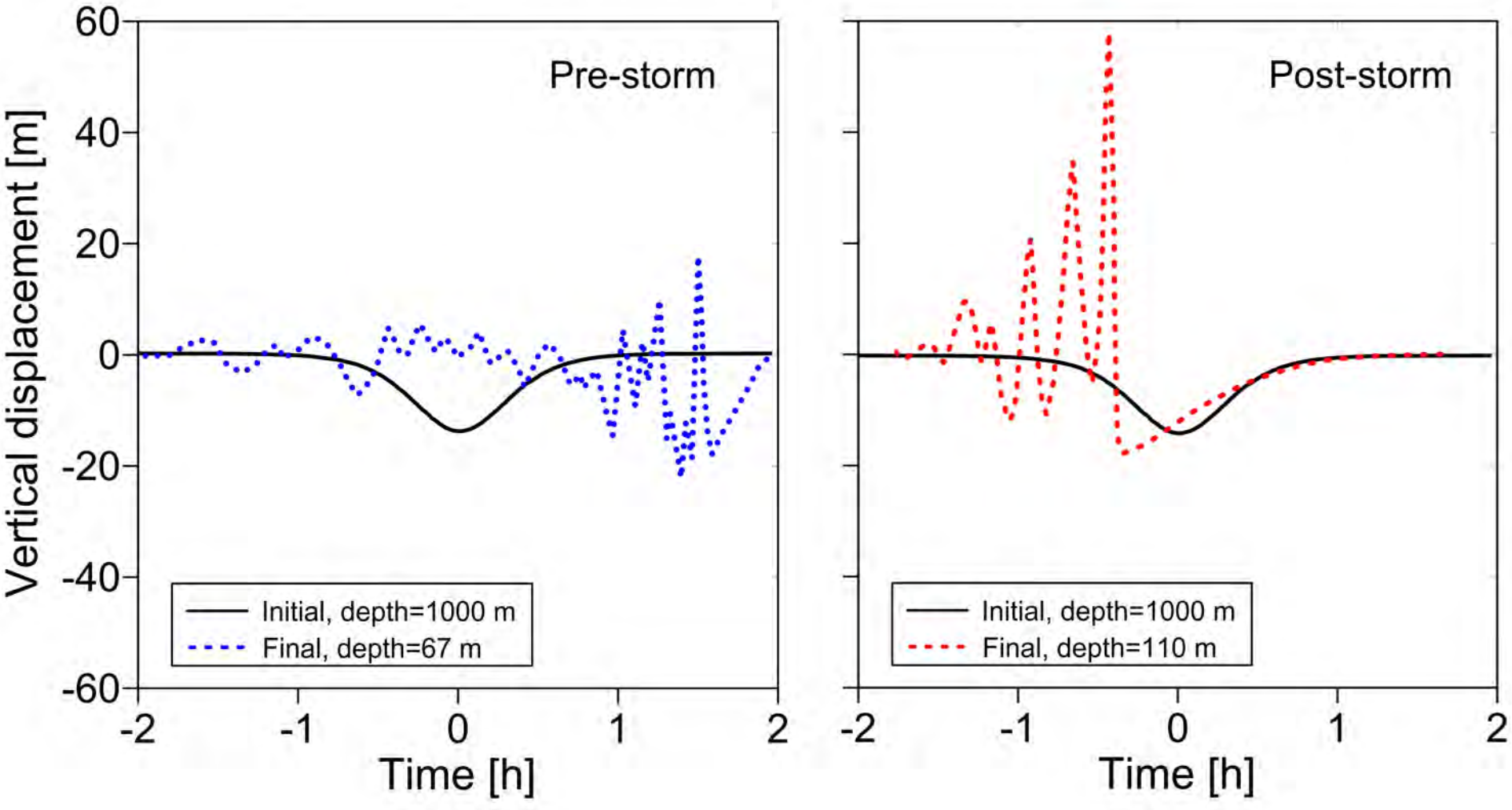
Pre-storm
Post-storm
Vertical displacement [m]
60
40
20
0
-20
-40
-60
-2
-1
0
1
2
Time [h]
Initial, depth=1000 m
Final, depth=67 m
Initial, depth=1000 m
Final, depth=110 m

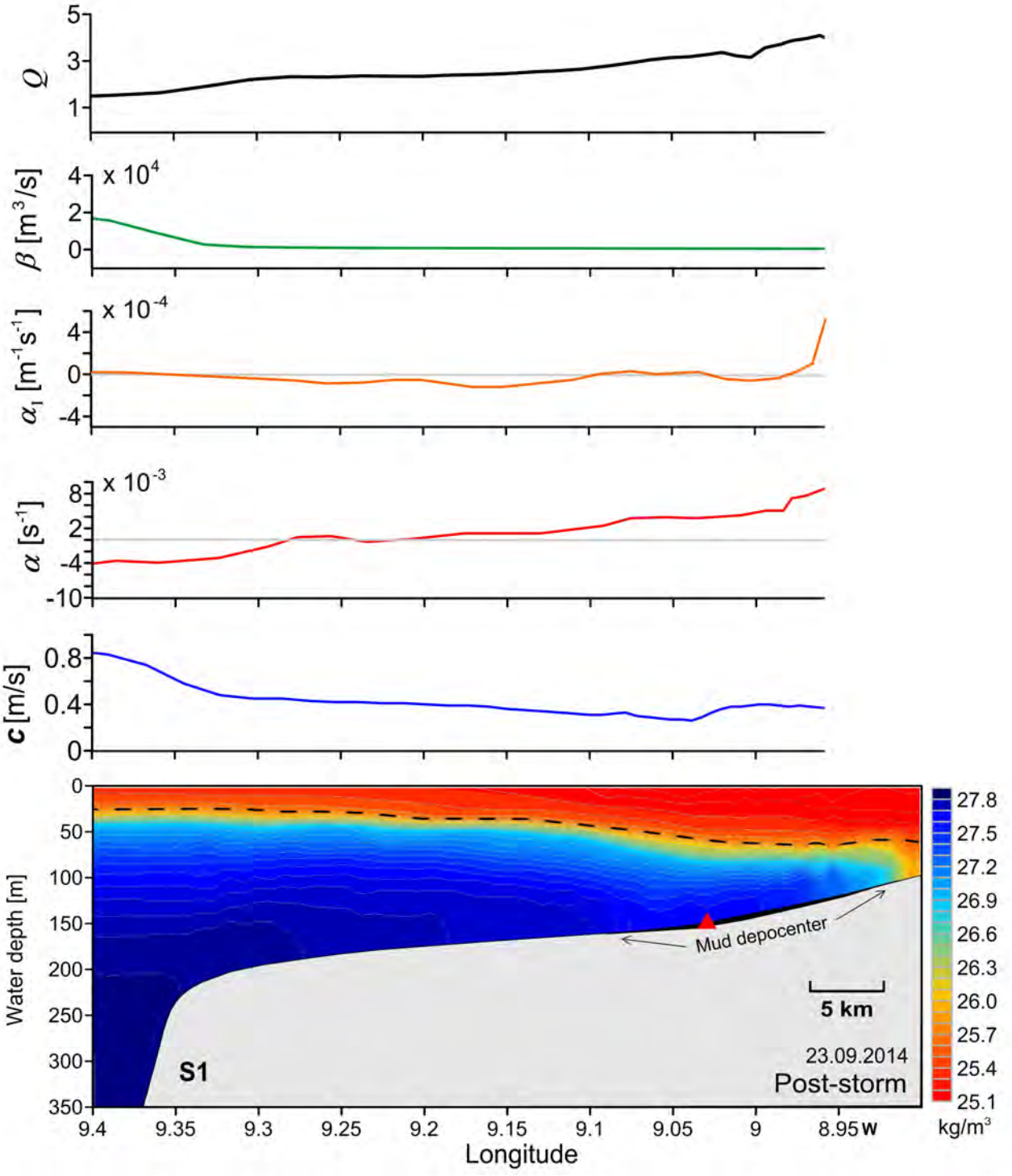
Q
5
3
1
β [m³/s]
x 10⁴
4
2
0
α₁ [m⁻¹s⁻¹]
x 10⁻⁴
4
0
-4
α [s⁻¹]
x 10⁻³
8
2
-4
-10
c [m/s]
0.8
0.4
0
Water depth [m]
0
50
100
150
200
250
300
350
Mud depocenter
5 km
S1
23.09.2014
Post-storm
9.4
9.35
9.3
9.25
9.2
9.15
9.1
9.05
9
8.95 W
Longitude
27.8
27.5
27.2
26.9
26.6
26.3
26.0
25.7
25.4
25.1
kg/m³

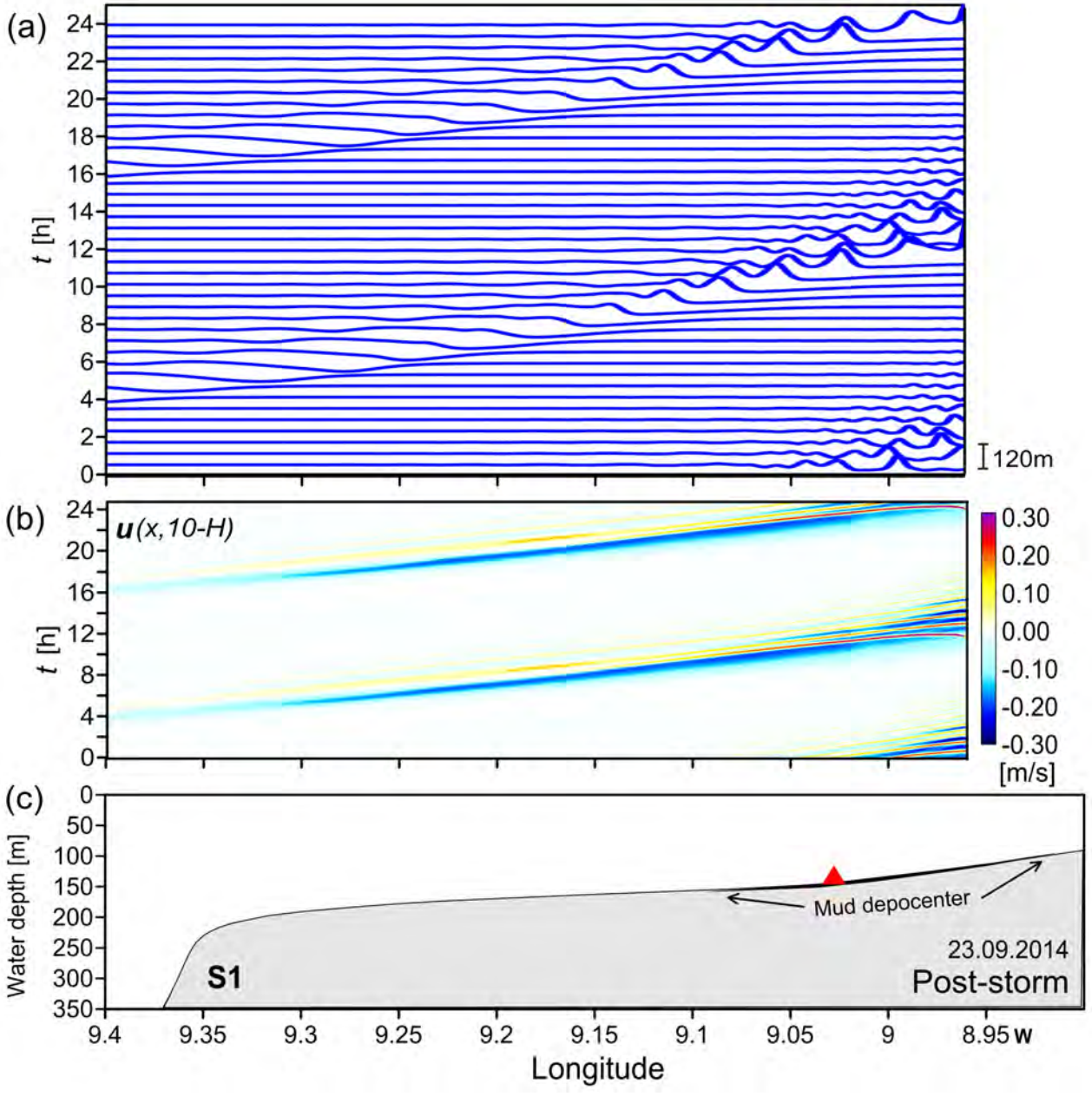
(a)
t [h]
120m
(b)
u(x,10-H)
t [h]
0.30
0.20
0.10
0.00
-0.10
-0.20
-0.30
[m/s]
(c)
Water depth [m]
Mud depocenter
S1
23.09.2014
Post-storm
9.4
9.35
9.3
9.25
9.2
9.15
9.1
9.05
9
8.95 W
Longitude

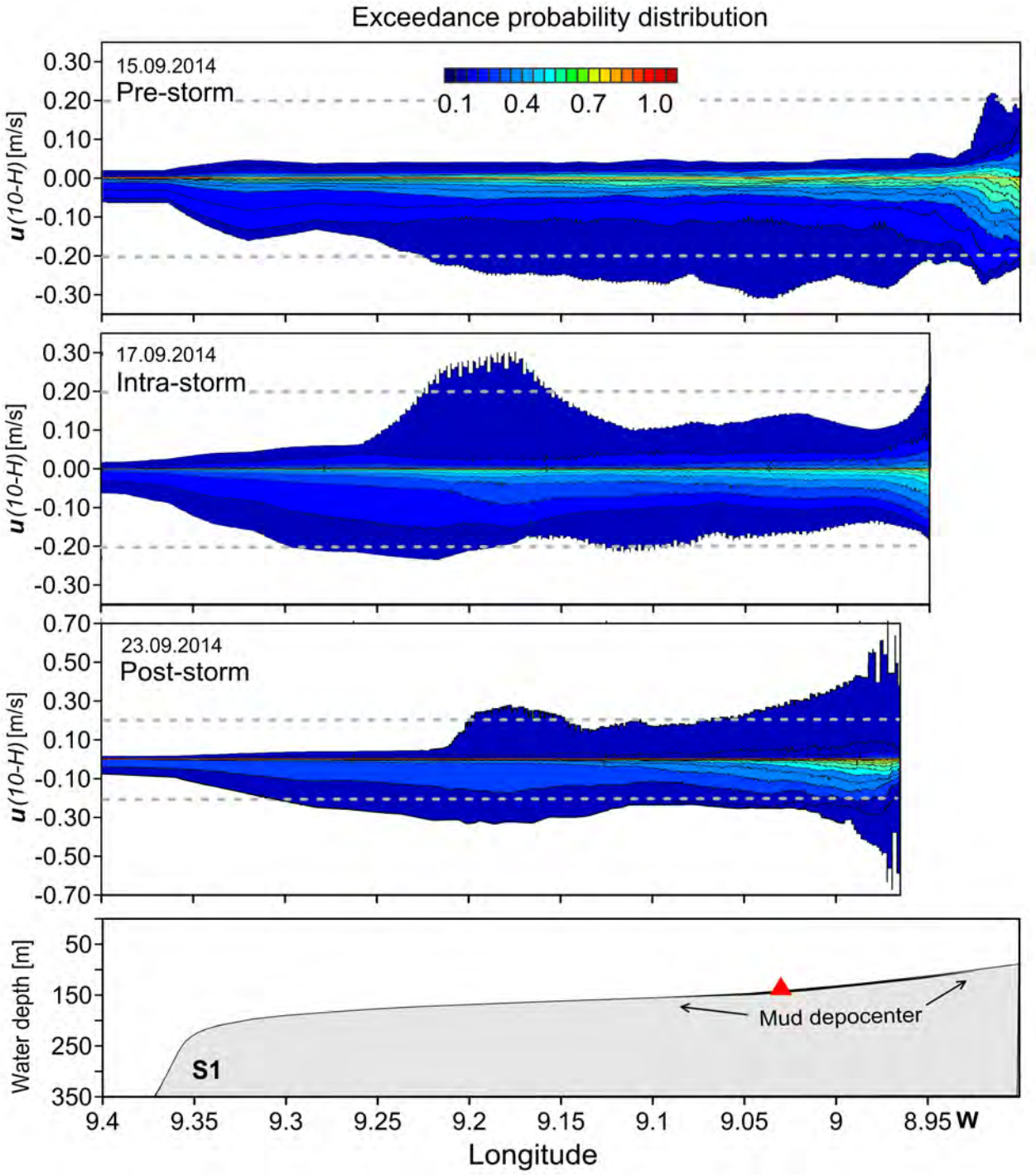
Exceedance probability distribution
15.09.2014
Pre-storm
0.1 0.4 0.7 1.0
u(10-H) [m/s]
17.09.2014
Intra-storm
23.09.2014
Post-storm
Water depth [m]
S1
Mud depocenter
Longitude
9.4 9.35 9.3 9.25 9.2 9.15 9.1 9.05 9 8.95 W

Supplementary Material for

Internal solitary waves control offshore extension of mud depocenters on the NW Iberian shelf

Wenyan Zhang[1,*], Ira Didenkulova[2,3], Oxana Kurkina[2], Yongsheng Cui[4], Julia Haberkern[5], Rebecca Aepfler[5], Ana I. Santos[6], and Till J.J. Hanebuth[7]

[[1] Institute of Coastal Research, Helmholtz-Zentrum Geesthacht, Germany]

[[2] Nizhny Novgorod State Technical University, Russia]

[[3] Department of Marine Systems, Tallinn University of Technology, Estonia]

[[4] The Center for Coastal Ocean Science and Technology, School of Marine Sciences, Sun Yat-sen University, China]

[[5] MARUM–Center for Marine Environmental Sciences, University of Bremen, Germany]

[[6] Marinha - Instituto Hidrográfico, Lisbon, Portugal]

[[7] Department of Coastal and Marine Systems Science, Coastal Carolina University, U.S.A.]

Introduction

The supplemental information provides descriptions of the background density fields for internal wave modeling (Supplement 1), model sensitivity to bias in the background density field (Supplement 2), simulation results of the shoreward propagation and transformation of internal solitary waves (ISW) in pre-storm (Supplement 3) and intra-storm periods (Supplement 4), respectively.

Supplement 1 - background density fields

The background density fields for the internal wave model are derived from simulation results by a validated 3D coastal ocean model (Zhang et al., 2016). A comparison between the simulation results and observed data (vertical CTD profiles) suggests an overall satisfactory model

performance (Fig. S1-c). Despite a deviation of the density gradient across the pycnocline, the temporal and spatial variation of both water layers (separated by the pycnocline) are well reproduced by the model. The deviation of the density gradient across the pycnocline is mainly related to an overestimation of the temperature beneath the pycnocline in the model, which is about 2 °C higher than the observed data (Zhang et al., 2016). It is worth to note that both 3D model results and observed data indicate a shoreward thickening of the surface water layer, meaning a deepening of the pycnocline from outer to inner shelf (Fig. S1). In addition, a rebound of bottom cold water pushed the front shoreward and upward shortly after the storm had passed. This significantly altered the stratification on the mid-shelf, especially on the MDC which was affected by the front during the storm.

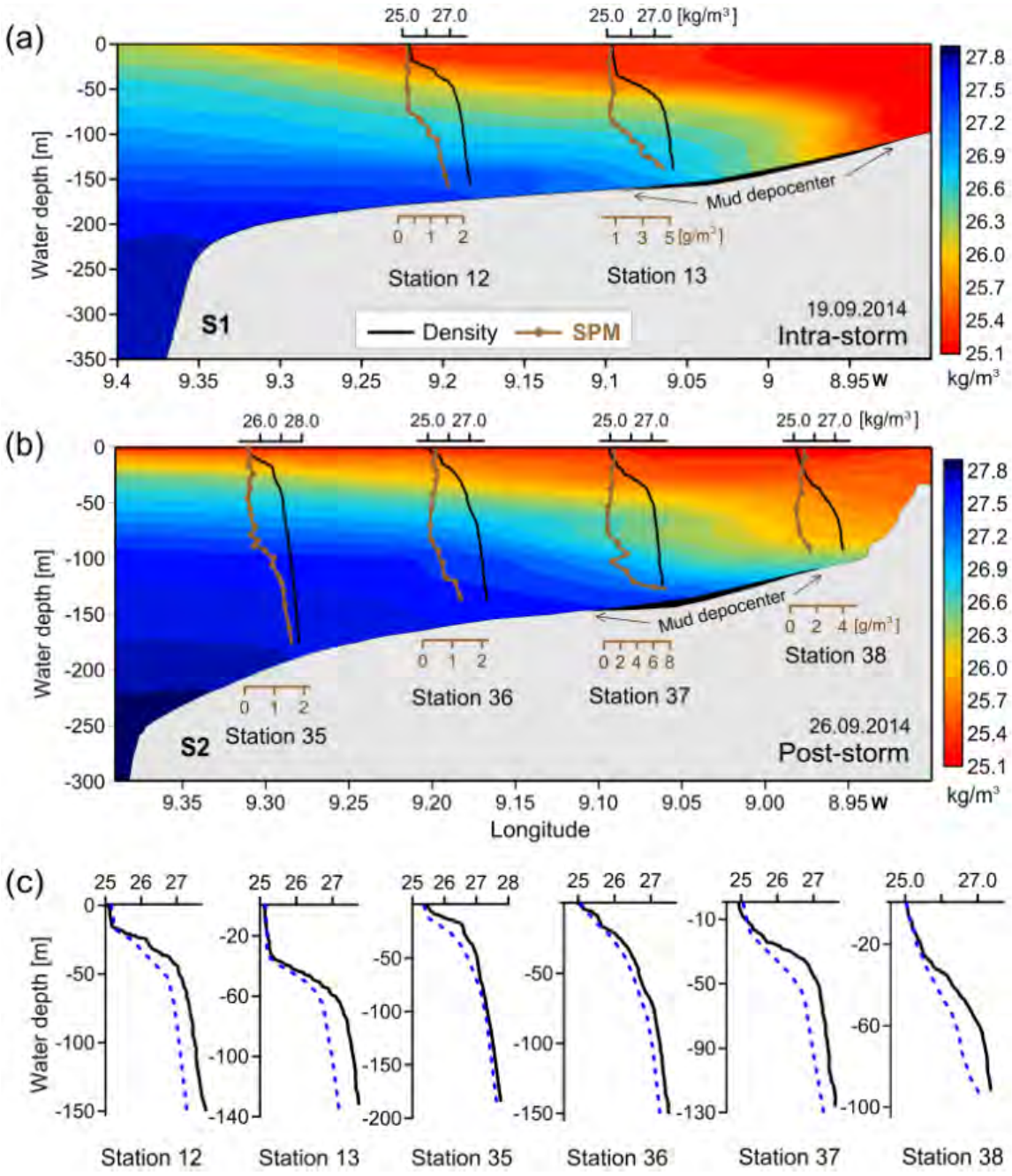

Figure S1. Comparison between modeled density fields (contour maps) and field measurements (CTD stations) across two track lines off the Ría de Vigo. Note that each CTD profiling terminates at 10 m above the seafloor and the sampling sequence goes from the shelf edge to the inner shelf. Vertical profiles of SPM concentration, calibrated by water samples *in situ*, are also shown at each station. The solid lines in (c) indicate observed water density profiles while the dashed lines represent model results. Unit of the horizontal axis in (c) is kg/m^3.

Supplement 2 - model sensitivity to bias in background density field

The effect of underestimating the density gradient across the pycnocline on the simulated ISWs can be roughly estimated by simplifying the water column to a two-layer system. In a two-layer system with a rigid lid and no background flow, the parameters (c, α, α_1, β and Q) and the modal structure function $\phi(z)$ in Eq. (1) can be quantified using the Boussinesq approximation:

$$c = \left[g(\rho_2 - \rho_1)h_1 h_2 / (\rho_1 h_2 + \rho_2 h_1)\right]^{1/2},$$

$$\alpha = 3c(\rho_2 h_1^{\,2} - \rho_1 h_2^{\,2}) / [2h_1 h_2 (\rho_2 h_1 + \rho_1 h_2)],$$

$$\alpha_1 = -3c\left[(\rho_1 h_2^2 - \rho_2 h_1^2)^2 + 8\rho_1 \rho_2 h_1 h_2 (h_1 + h_2)^2\right] / [8h_1^2 h_2^2 (\rho_1 h_2 + \rho_2 h_1)^2],$$

$$\beta = ch_1 h_2 (\rho_2 h_2 + \rho_1 h_1) / [6(\rho_2 h_1 + \rho_1 h_2)],$$

$$Q = 1/\left[2gc(\rho_2 - \rho_1)\right]^{1/2},$$

$$\phi(z) = \begin{cases} -z/h_1, & \text{if } 0 > z > -h_1 \\ (z+H)/h_2, & \text{if } -h_1 > z > -H \end{cases},$$

where h_1 and h_2 are the thickness of the upper and lower layer, respectively, ρ_1 and ρ_2 are the corresponding densities. It can be seen from the above formula that five parameters (c, α, α_1, β and Q) are affected by the difference between ρ_1 and ρ_2, while $\phi(z)$ is not. An underestimation of $\rho_2 - \rho_1$ by ~16% in our density field compared to the field data results in an underestimation of c by ~8% and subsequently affects the other three parameters α, α_1 and β to a similar extent, while Q is overestimated by ~14%. It can be easily justified that in most circumstances such bias in the parameters do not influence the model results significantly, unless $h_1 \approx h_2$. In this case a subtle change in $\rho_2 - \rho_1$ would cause a change in the sign of α. Because $\alpha_1 < 0$ when $h_1 \approx h_2$, the polarity of the ISWs is determined by the sign of α. To conclude, the polarity of the ISWs is quite sensitive to a change of $\rho_2 - \rho_1$ when $h_1 \approx h_2$, which might have a consequence on the transport of sediment. However, it should be noted that $h_1 \approx h_2$ normally

occurs in a small part of the shelf only (e.g. between 9°W and 8.95 °W in the post-storm period, as shown in Fig. 9), and most importantly, it does not affect the continuing transformation of the ISWs. An underestimation of $\rho_2 - \rho_1$ also has an effect on the amplitude of the ISWs (see for example, Eq. (14) in Grimshaw et al. (2004)). In our case this slightly reduces the amplitude of the ISWs by ~11%. In summary, although an underestimation of $\rho_2 - \rho_1$ by ~16% in our density field would affect the polarity and amplitude of the ISWs under certain circumstances, the general validity of our model results is not violated.

Supplement 3 - simulated internal waves in pre-storm conditions

The spatial variation of the coefficients in the 2DV model along Profile S1 in the pre-storm period is shown in Fig. S2. The model computation terminates on the inner shelf (~8.9°W) close to the shoreward margin of the mud depocenter. The amplitude of the coefficient of the cubic nonlinearity (α_1) remains constantly small ($\pm 2 \times 10^{-4}$ $m^{-1}s^{-1}$) along the propagation of the ISW from the slope to the mid-shelf, despite that the sign of α_1 changes several times. After reaching the inner part of the depocenter at 8.93°W, the amplitude of α_1 increases drastically and the corresponding cubic nonlinear term ($\alpha_1 \eta^2$) overwhelms the linear term (c). In the entire course of propagation before the possible breaking point (i.e., where the computation terminates), the coefficient of the quadratic nonlinearity α remains negative. After passing 8.93°W, α starts to rise rapidly and reaches zero at the place where the computation terminates. The spatial variation of the quadratic ($\alpha\eta$) and cubic ($\alpha_1 \eta^2$) nonlinear term and their comparison with the linear term (c) indicate that the shoaling and transformation of the ISW from the slope to mid-shelf (before approaching 8.93°W) are mainly controlled by the linearity and secondarily influenced by the quadratic nonlinearity, with c about 2.5 to 6 times larger than $\alpha\eta$.

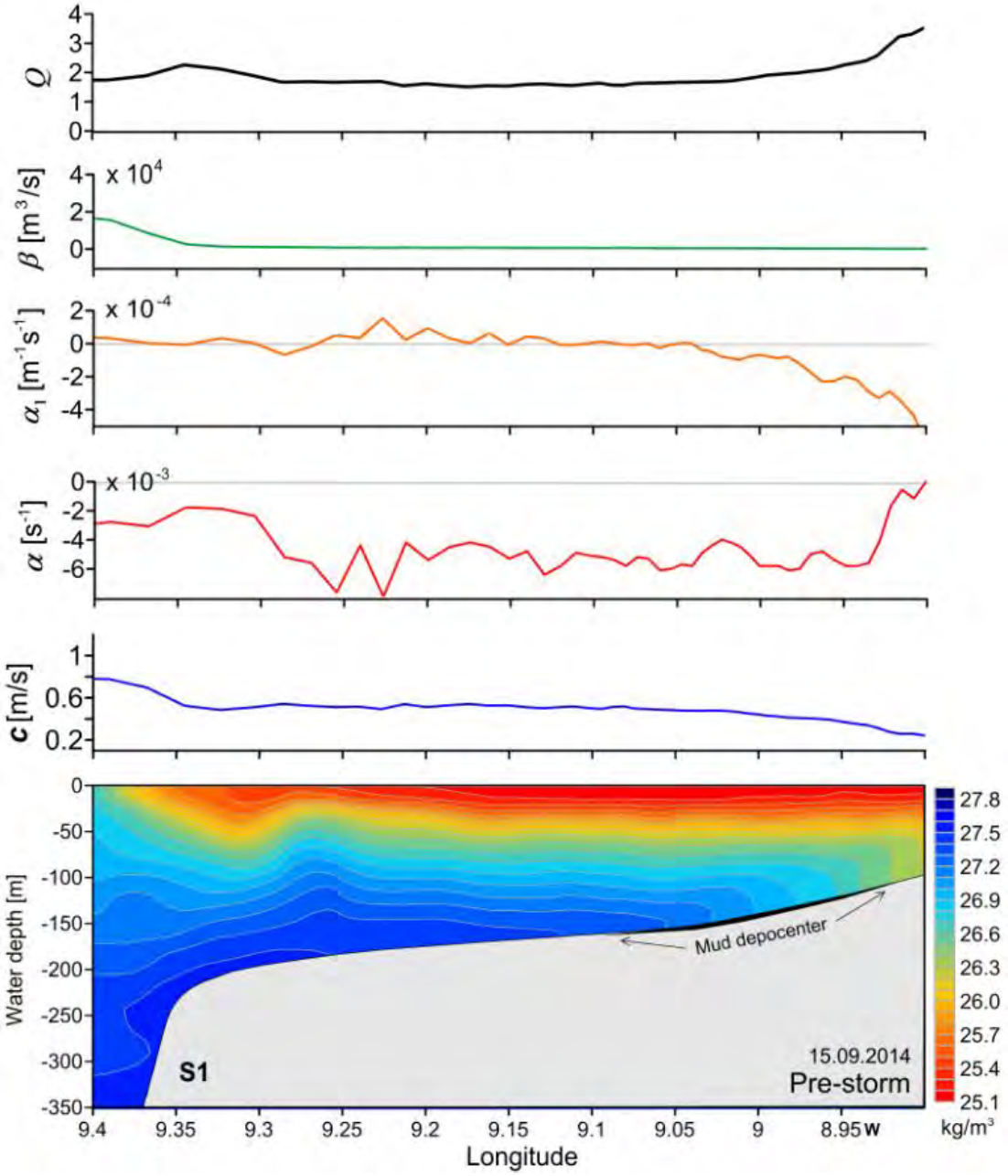

Figure S2. Spatial variation of coefficients of the 2DV model along Profile S1 in the pre-storm period. The background density field is shown in the bottom panel. Note that the model domain starts from the continental slope (-1000 m), which is not shown here for better representation of the mid-shelf. Model computation terminates at the place where high order nonlinearity (i.e., the quadratic and cubic nonlinear terms) takes control and the weakly nonlinear assumption is no longer valid.

Because of a dominance of linearity in the initial propagation stage, the ISW remains in the soliton-like shape until reaching the upper slope (-700 m water depth), and starts deformation afterwards (Fig. S3). The ISW slightly increases its amplitude from 15 to 17 m during the first 18 km of propagation until it reaches above the upper slope (-700 m water depth), and then increases with an accelerated rate in the next 7 km until reaching the shelf edge at -300 m where its amplitude increases to 26 m. A lengthening trailing tail starts to develop behind the leading wave above the shelf edge (-300 m) and a dispersive wave packet forms there. Because part of the energy in the initial internal wave is lost to the trailing tail, the amplitude of the leading wave decreases from 26 m to 20 m in the next 5 km from the shelf edge towards the coast. The leading wave propagates faster (larger than the local linear long wave speed c) than the trailing waves which have the phase speed of c. The negative polarity is maintained in the leading ISW during its propagation from the shelf edge to the mid-shelf until reaching 8.93°W. In the meanwhile a trailing packet with positive polarity develops right behind the leading ISW. The wave length of the trailing packet becomes continuously smaller due to a conservation of energy, while the amplitude becomes increasingly larger. After passing 8.93°W, the amplitude of the trailing waves increases drastically and reaches a maximum (~40 m) at 8.9°W where the model computation terminates. Breaking and intense mixing should occur in the shoreward direction of the large amplitude waves, according to the criteria used in this study (see the main text for further details), i.e., the local Ostrovsky number ($O_s = 2\alpha^2\eta^2 c\beta^{-1} f^{-2}$) exceeds 1 and the maximum horizontal orbital velocity $u(x,z)$ exceeds the wave phase speed c (Fig. S2 and S3). Correspondingly, the near-bottom horizontal orbital velocity $u(x,10-H)$ of the ISW increases in an accelerated rate after passing 8.93°W, where the seafloor depth is -106 m, and reaches 0.27 m/s before likely breaking. This is induced by a combined effect of increased amplitude (η) and vertical gradient of the modal structure function $\phi(z)$. An asymmetry in both the strength of $u(x,10-H)$ and duration of the orbital excursion, with a more pronounced offshore directed

component, is clearly seen (Fig. S3). As pointed out in the main text, the asymmetry in the duration of the orbital excursion is attributed to deformation of the ISW during its shoaling, which results in a narrowing of the wave crest and broadening of the wave trough.

If we adopt the critical shear stress for resuspension of unconsolidated silts and very fine sands as 0.1 Pa, it can be seen from the result (Fig. S3) that the ISW is mostly below the threshold until breaking. This result indicates that the ISW in the pre-storm period mainly act as agency for transporting instead of resuspending sediment from the mud depocenter.

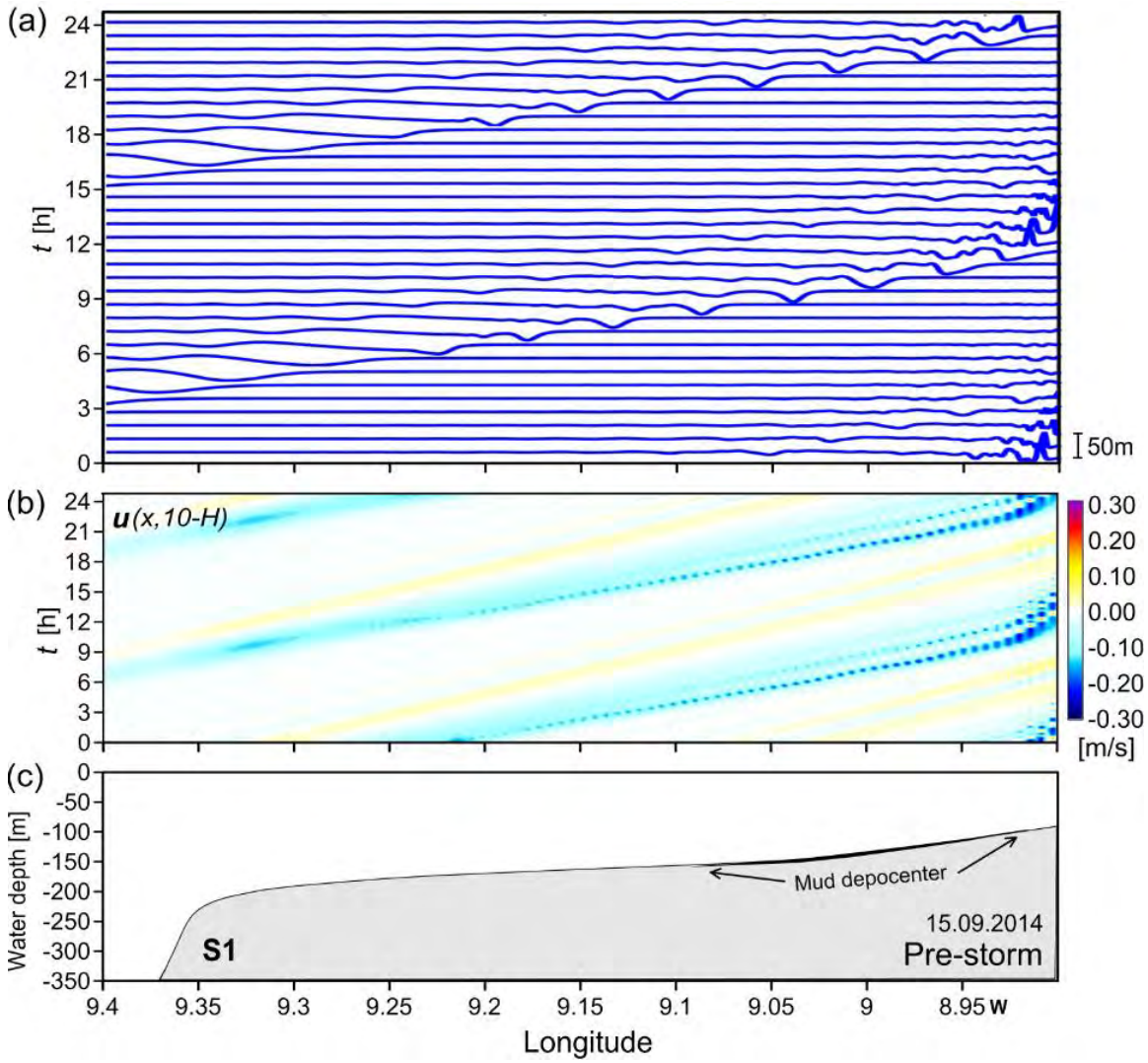

Figure S3. (a) Evolution of a periodic ISW (initial amplitude = 15 m) along Profile S1 in the pre-storm period. (b) Near-bottom horizontal orbital velocity $u(x,10-H)$ associated with the ISW. Positive values indicate shoreward direction. (c) Topography of the shelf along Profile S1.

Supplement 4 - simulated internal waves in intra-storm conditions

The spatial variation of the coefficients in the 2DV model along Profile S1 during the storm period is shown in Fig. S4. The model computation terminates on the inner shelf (~8.95°W) at the shoreward margin of the mud depocenter. The coefficient of the cubic nonlinearity α_1 is initially positive and small ($< 5 \times 10^{-5}$ $m^{-1}s^{-1}$). After reaching above the shelf edge (-300 m), α_1 changes its sign to negative and remains the sign during the major course of propagation until approaching 8.964°W (-107 m), afterwards it rises quickly until likely breaking. Different from the case in the pre-storm period in which the coefficient of the quadratic nonlinearity α remains mostly negative, α in the intra-storm period is quite variable and changes its sign several times during the propagation of the ISW. Because α_1 remains negative, the polarity of the ISW is exclusively determined by the sign of α on the shelf, as shown in Fig. S5.

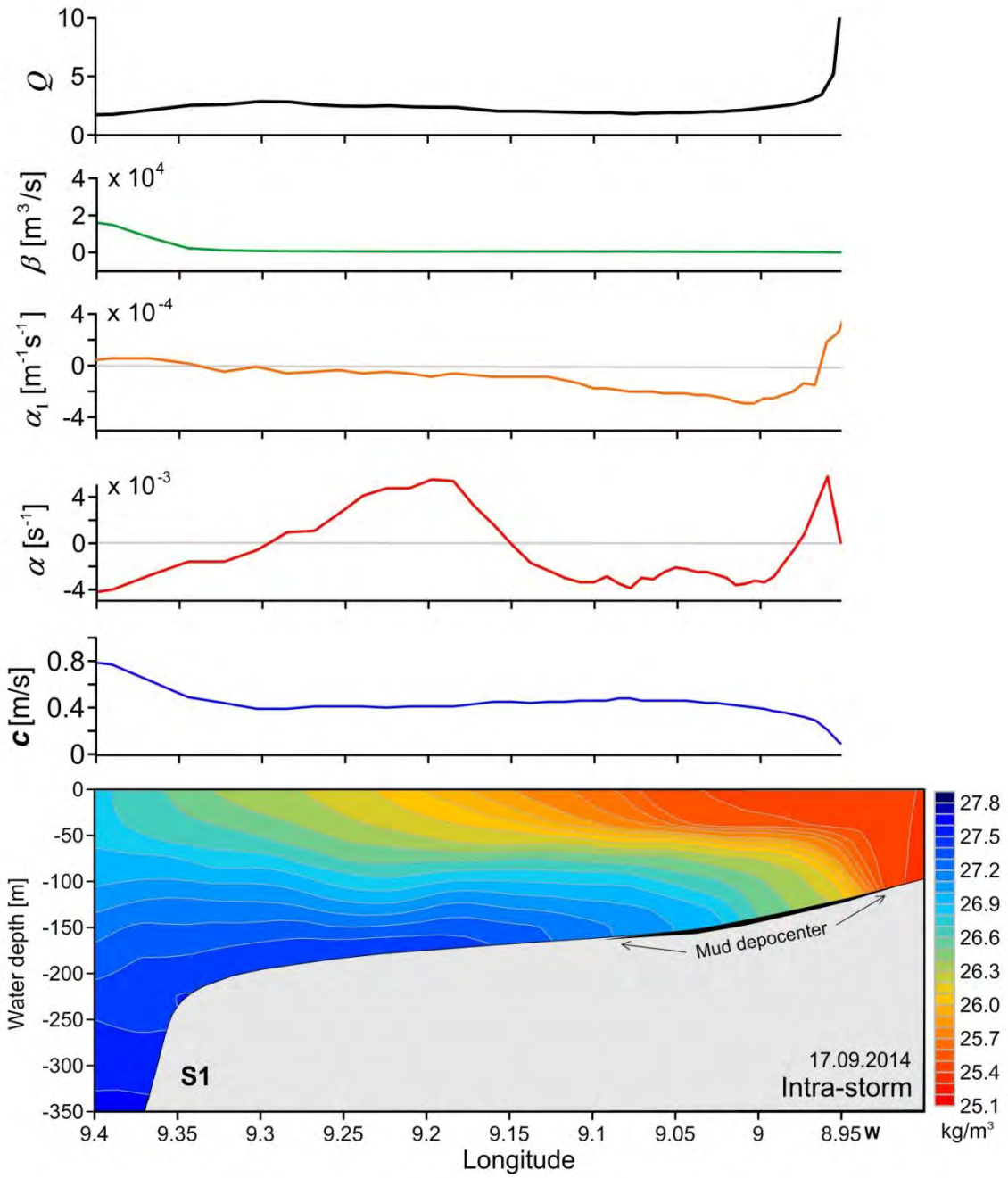

Figure S4. Spatial variation of coefficients of the 2DV model along Profile S1 during the storm. The background density field is shown in the bottom panel. Note that the model domain starts from the continental slope (-1000 m), which is not shown here for better representation of the mid-shelf. Model computation terminates at the place where high order nonlinearity (i.e., the quadratic and cubic nonlinear terms) takes control and the weakly nonlinear assumption is no longer valid.

Similar to the case in the pre-storm period, the ISW remains in the soliton-like shape in the initial propagation stage until reaching the upper slope (-700 m water depth), and starts deformation afterwards (Fig S5). The ISW mildly increases its amplitude from 15 to 20 m in the first 25 km of propagation from the open boundary (-1000 m) to the shelf edge (-300 m). After passing the shelf edge an accelerated increase of amplitude of the leading wave is seen from the result. A local maximum of 30 m in the amplitude is reached at the outer shelf (9.22°W). Correspondingly, the near-bottom horizontal orbital velocity $u(x,10-H)$ of the leading wave is enhanced and reaches the magnitude of 0.3 m/s at the outer shelf (9.22°W). Interestingly, the amplitude of the leading ISW decreases after passing the local maximum point at 9.22°W. Its value declines to 21 m when approaching the outer margin of the mud depocenter (9.1°W). As a result $u(x,10-H)$ decreases below 0.2 cm/s. Along the propagation a trailing tail with increasing number of waves develops. The asymmetry in duration of the orbital excursion is less prominent in this case compared to the pre-storm period (Fig. S5 and see also Fig. 11 in the main text), although the offshore transport in general still dominates. After passing a major part of the mud depocenter the leading wave increases the amplitude in an accelerated rate from 8.97°W, and reaches 31 m before its likely breaking at 8.95°W.

Again, assuming the critical shear stress for resuspension of unconsolidated silts and very fine sands is 0.1 Pa, it can be seen from the result (Fig. S5) that the ISW get strong enough to resuspend sediment from the outer shelf (between 9.17° and 9.3°W). Their impact on the mud depocenter is relatively small due to reduced $u(x,10-H)$.

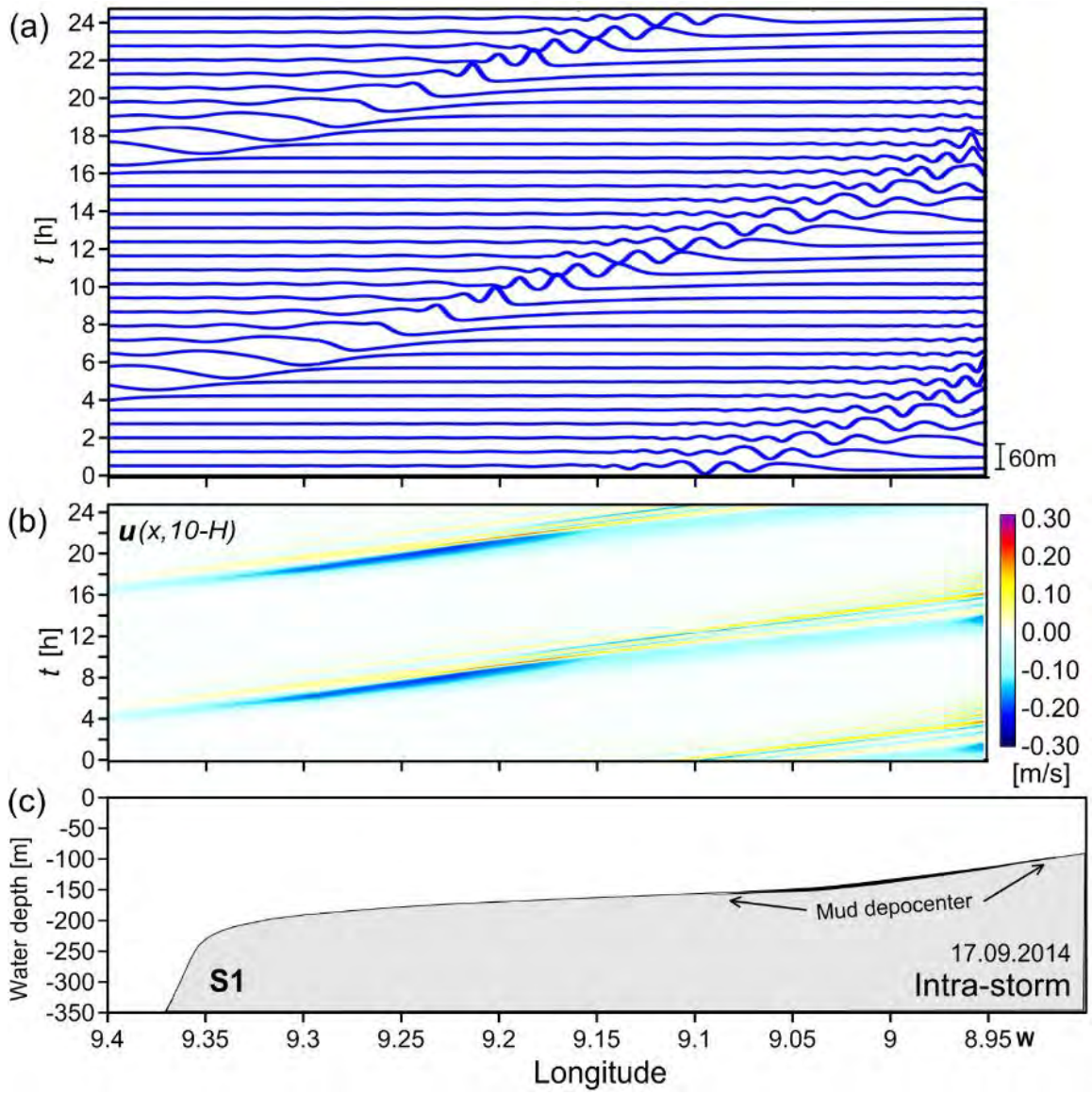

Figure S5. (a) Evolution of a periodic ISW (initial amplitude = 15 m) along Profile S1 during the storm. (b) Near-bottom horizontal orbital velocity $u(x,10-H)$ associated with the ISW. Positive values indicate shoreward direction. (c) Topography of the shelf along Profile S1.